Satellite-based radiative forcing by light-absorbing particles in snow across the Northern Hemisphere

Jiecan Cui[1], Tenglong Shi[1], Yue Zhou[1], Dongyou Wu[1], Xin Wang[1,2] and Wei Pu[1]

[1]Key Laboratory for Semi-Arid Climate Change of the Ministry of Education, College of Atmospheric Sciences, Lanzhou University, Lanzhou 730000, China

[2]Institute of Surface-Earth System Science, Tianjin University, Tianjin 300072, China

Corresponding author: Wei Pu (puw09@lzu.edu.cn)

Abstract. Snow is the most reflective natural surface on Earth and consequently plays

an important role in Earth's climate. Light-absorbing particles (LAPs) deposited on the

snow surface can effectively decrease snow albedo, resulting in positive radiative

forcing. In this study, we used remote sensing data from NASA's Moderate Resolution

Imaging Spectroradiometer (MODIS) and the Snow, Ice, and Aerosol Radiative

(SNICAR) model to quantify the reduction in snow albedo due to LAPs, before

validating and correcting the data against in-situ observations. We then incorporated

these corrected albedo-reduction data in the Santa Barbara DISORT Atmospheric

Radiative Transfer (SBDART) model to estimate Northern Hemisphere radiative

forcing except for midlatitude mountains in December-May for the period 2003–2018.

Our analysis reveals an average corrected reduction in snow albedo ($\Delta\alpha_{MODIS,corrected}^{LAPs}$)

of ~0.021 under all-sky condition, with daily radiative forcing ($RF_{MODIS,daily}^{LAPs}$) values

of ~2.9 W m^{-2}, over mapped snow-covered area in Northern Hemisphere. We also

observed significant spatial variations in $\Delta\alpha_{MODIS,corrected}^{LAPs}$ and $RF_{MODIS,daily}^{LAPs}$, with

the lowest respective values (~0.016 and ~2.6 W m^{-2}) occurring in the Arctic and the

highest (~0.11 and ~12 W m^{-2}) in northeastern China. From MODIS retrievals, we

determined that the LAP content of snow accounts for 84% and 70% of the spatial

variability in albedo reduction and radiative forcing, respectively. We also compared

retrieved radiative forcing values with those of earlier studies, including local-scale

observations, remote-sensing retrievals, and model-based estimates. Ultimately,

estimates of radiative forcing based on satellite-retrieved data are shown to represent

true conditions on both regional and global scales.

1. Introduction

Seasonal snow cover affects 30% of Earth's land surface and exerts a cooling influence on global climate through its direct interaction with the surface radiances budget (Painter et al., 1998; Flanner et al., 2011). However, snow surface darkening due to light-absorbing particles (LAPs) such as black carbon (BC), organic carbon (OC), dust, and algae, can significantly alter the reflective properties of snow (Warren, 1982, 1984; Hadley and Kirchstetter, 2012). When deposited on the snow surface, LAPs increase the absorption of solar radiances (Painter et al., 2012a; Liou et al., 2014; Dang et al., 2017), thereby reducing the snow albedo (Warren and Brandt, 2008; Kaspari et al., 2014). As a result, radiative forcing of LAPs in snow (RFLS) plays a critical role in snow-cover decline on both regional and global scales (Warren and Wiscombe, 1980), perturbing the climate system and impacting hydrological cycles (Qian et al., 2011).

One of the primary LAPs, BC, is derived from the incomplete combustion of fossil fuels and biomass (Bond et al., 2013; Dang et al., 2015) and is second only to CO_2 in its contribution to climate forcing (Hansen and Nazarenko, 2004; Ramanathan and Carmichael, 2008; Bond et al., 2013). Yet, despite considerable efforts to measure the BC content of Northern Hemisphere snow and ice (Doherty et al., 2010, 2014; Huang et al., 2011; Ye et al., 2012; Wang et al., 2013b, 2017), the inherent challenges presented by a temporospatially variable snow cover mean our understanding of LAPs in snow is far from complete. As a result, persistent uncertainties remain in regional and global-scale RFLS estimates based on field measurements (Zhao et al., 2014).

Several previous investigations have utilized numerical models to estimate RFLS, including that of Hansen and Nazarenko (2004), who concluded that BC in snow and ice exerts a positive climate forcing throughout the Northern Hemisphere of +0.3 W m^{-2}, or explaining approximately one quarter of observed global warming. More recently, Flanner et al. (2007) employed an aerosol/chemical-transport general-circulation model, coupled with the Snow, Ice, and Aerosol Radiative (SNICAR) model (Flanner et al., 2007; 2009), to estimate globally averaged radiative forcing values of +0.054 (range 0.007–0.13) and +0.049 (0.007–0.12) W m^{-2} for a strong (1998) and weak (2001) boreal fire year, respectively. Using the Weather Research and Forecasting (WRF) model (Skamarock et al., 2008) coupled with a chemistry component (Chem) (Grell et al., 2005) and SNICAR modeling, Zhao et al. (2014) demonstrated that RFLS over northern China in January–February 2010 was ~10 W m^{-2}. However, despite their potentially valuable contribution, climate models contain significant uncertainties in representations of LAP emissions, transport, deposition, and post-depositional processes that can propagate into simulations of LAP concentrations and their climate forcing (Qian et al., 2015; Lee et al., 2016). Zhao et al. (2014) also confirmed that, relative to observational data, modeled LAPs and radiative forcing estimates exhibit biases that are difficult to explain and quantify. These shortcomings underscore the need for a refined approach to estimating real-time RFLS that minimizes the mismatch between field observations and model simulations.

In addition to modeling, remote sensing has been used to assess the physical

1 characteristics of snow cover (Nolin and Dozier, 1993, 2000; Painter et al., 2009, 2012a,

2 2013; Miller et al., 2016). Nolin and Dozier (2000), for example, retrieved grain-size

3 data from satellite-derived reflectance at near-infrared (NIR) wavelengths, following

4 the rationale that snow-grain size, in conjunction with solar zenith angle, dictates the

5 path-length of penetrating photons (Wiscombe and Warren, 1980) and thus influences

6 albedo in the NIR. Similarly, recent studies have attempted to employ satellite-derived

7 snow albedo at visible (VIS) wavelengths to retrieve RFLS data (Seidel et al., 2016; Pu

8 et al., 2019). Briefly, this retrieval method exploits the imaginary component of the

9 complex refractive index for ice (K_{ice}), which is very low at VIS wavelengths and

10 results in the extremely high VIS albedo for pure snow. In contrast, the imaginary

11 component of the complex refractive index for LAPs (K_{LAPs}) at VIS wavelengths is

12 orders of magnitude greater, resulting in the reduction in VIS snow albedo (Wiscombe

13 and Warren, 1980). Moreover, albedo variability at VIS wavelengths is dominated by

14 even minor concentrations of LAPs (Brandt et al., 2011; Painter et al., 2012b).

15 Painter et al. (2012a) employed surface-reflectance data provided by NASA's Moderate

16 Resolution Imaging Spectroradiometer (MODIS) for the Upper Colorado River Basin

17 and Hindu Kush-Himalaya (HKH) to make the first quantitative, remote-sensing-based

18 retrievals of instantaneous surface radiative forcing (RF) due to LAPs. Relative to the

19 Western Energy Balance of Snow (WEBS) network (Painter et al., 2007), that study

20 established that MODIS-derived radiative forcing exhibits a positive bias at lower RF

21 values and a slightly negative bias at higher values. A more recent study by Seidel et al.

(2016) used remote sensing to constrain instantaneous melt-season RFLS values of 20–

200 W m^{-2} for the Sierra Nevada and Rocky Mountains, while Pu et al. (2019) reported

MODIS-derived values of 22–65 W m^{-2} for northern China in January–February

(regional average ~45 W m^{-2}). Acknowledging this demonstrated efficacy of remote

sensing retrievals for establishing RFLS on regional scales, we note this approach has

so far not captured spatial variability in RFLS on a global scale.

In this study, we employed MODIS data to determine the reduction in Northern

Hemisphere snow albedo due to LAPs. Retrievals were validated and corrected

according to ground-based snow observations, after which spatial variability in albedo

reduction and radiative forcing over mapped snow-covered area in Northern

Hemisphere were assessed quantitatively. Finally, we compared our satellite-derived

radiative forcing values with the modeling results of CESM2 (Eyring et al., 2016;

Danabasoglu et al., 2020). Despite the persistence of non-negligible uncertainties and

biases, our satellite-based retrievals constitute the first hemisphere-scale assessment of

RFLS and provide valuable information for improving climate model simulations.

2. Data

2.1. Remote-sensing data

To investigate the impact of LAPs on snow albedo, we utilized the following MODIS

data sets: surface albedo (MCD43C3; 0.05° × 0.05° resolution), snow cover

(MYD10C1; 0.05° × 0.05° resolution), land cover type (MCD12C1; 0.05° × 0.05°

resolution), and atmospheric parameters (MYD08_D3; 1° × 1° resolution). Each data

set corresponds to December-May for the period 2003–2018 (https://earthdata.nasa.gov, last access: 20 January 2019). MCD43C3 is the daily combined MODIS output derived from both the Terra and Aqua satellites, and provides black-sky albedo (directional hemispherical reflectance, DHF) and white-sky albedo (bi-hemispherical reflectance, BHF) at local solar noon for bands 1–7 (band 1, 620–670 nm; band 2, 841–876 nm; band 3, 459–479 nm; band 4, 545–565 nm; band 5, 1230–1250 nm; band 6, 1628–1652 nm; band 7, 2105–2155 nm), as well as values for quality control, local noon solar zenith angle, and associated parameters. MCD43C3 observations are weighted to estimate albedo on the 9th day of each 16-day period and have been corrected for the influence of local slope and aspect, atmospheric gases, and aerosols.

Snow-cover data are provided daily by MYD10C1 as a report of the snow-cover fraction (SCF), derived from the Normalized Difference Snow Index (NDSI). MCD12C1 provides a spatially aggregated and reprojected land-cover type, which is derived from the supervised classification of MODIS reflectance data, while MODIS MYD08_D3 reports values of solar azimuth angle.

Average-daily solar radiances and cloud fraction were obtained from NASA's Clouds and the Earth's Radiant Energy System (CERES: https://ceres.larc.nasa.gov, last access: 12 April 2019), part of the Earth Observing System comprising the Aqua, Terra, and S-NPP satellites. CERES provides instantaneous measurements of solar radiances, which are then converted to average-daily flux by angular dependence and empirical diurnal albedo modeling as the satellite passes through the point of descent (Doelling et al.,

2013; Su et al., 2015; Loeb et al., 2018). We used the total downward shortwave flux

and cloud fraction at the surface, provided by the "CERES Single Scanner Footprint

1.08 (SSF1deg)" product, to estimate average-daily RFLS under all-sky conditions.

Shuttle Radar Topography Mission (SRTM) digital elevation data are provided by the

US Geological Survey (https://www.usgs.gov/, last access: 9 December 2018) to adjust

slope- and aspect-induced changes of surface solar irradiance in complex terrain. The

spatial resolution of SRTM data for the Northern Hemisphere is 30 m.

2.2. Snow depth data

Estimates of snow depth were obtained from the European Centre for Medium-Range

Weather Forecasts (ECMWF) Interim Re-Analysis (ERA-Interim)

(https://www.ecmwf.int, last access: 15 January 2019). ERA-Interim is a new

generation of reanalysis based on a 12-hourly and 4-dimensional variational data

assimilation (4D-Var) covering the period 1979–present. ERA-Interim performs better

in model physics frameworks, data quality control, and background error criteria than

previous versions (Berrisford et al., 2011; Brun et al., 2013). In this study, we used

snow-water equivalent (SWE) data for December-May covering the period 2003–2018.

These data were generated by forecast models and updated according to a Cressman

analysis of snow observations (Drusch et al., 2004; Dee et al., 2011). We note that the

previous occurrence of false snow-free patches, arising from application of Cressman

analysis in regions of sparse ground control, has been mitigated by ECMWF upgrades

(Dee et al., 2011). Finally, SWE is converted to snow depth by assuming that average

1. December-May snow density is ~300 kg m^{-3}, consistent with snow-depth estimates by

2. the Canadian Meteorological Centre (CMC) (Sturm et al., 1995; Brown and Mote,

3. 2009).

4. **2.3. In-situ measurements of LAPs in snow**

5. To correct the satellite retrievals, we collected a comprehensive set of in-situ

6. measurements of BC concentrations from the field campaigns in the Arctic in spring of

7. 2005-2009 (Doherty et al., 2010), North America in January-March of 2013 (Doherty

8. et al., 2014), Northern China in January-February of 2010, 2012 and 2014 (Ye et al.,

9. 2012; Wang et al., 2013; Wang et al., 2017). The BC concentrations are measured by

10. the two-sphere integrating-sandwich (TSI) spectrophotometer in the Arctic, North

11. America, and Northern China (Grenfell et al., 2011; Wang et al., 2020). Briefly, TSI

12. produces a diffuse radiation field when the white light illumination is transmitted into

13. an integrating sphere; then the diffuse radiation passes through the filter and is detected

14. by a spectrometer. The TSI technique acquires the light attenuation spectrum due to the

15. LAPs loaded on the sample filter (Grenfell et al., 2011). Then, the light attenuation

16. spectrum of the sample filter is transformed into an equivalent BC mass (unit: g cm^{-2})

17. loading by comparing against the standard filters. The equivalent BC has been defined

18. by Doherty et al. (2010) which briefly as the amount of BC in the snow to account for

19. the wavelength-integrated total light absorption in the wavelengths of 300-750 nm by

20. all particulate constituents. In this study, we used BC_{equiv} for all LAPs to calculate the

21. in-situ snow albedo reduction and radiative forcing (Fig. S3).

2.4. Climate model simulations

We compared our remotely sensed retrievals of daily-average RFLS for the 2003–2014 study period with simulated results derived from CESM2 (https://esgf-node.llnl.gov/, last access: 15 July 2019). In this study, we employed simulations of snow BC concentrations derived from the CESM2 historical experiments, in conjunction with ERA-Interim SWE, MODIS-retrieved snow grain-size, and CERES total downward shortwave flux data under all-sky condition, to model daily-average RFLS for the study period. Simulations were performed using the Snow, Ice, and Aerosol Radiative (SNICAR) and Santa Barbara DISORT Atmospheric Radiative Transfer (SBDART) models, and the model output was compared with satellite-based retrievals.

3. Methods

3.1. Radiative transfer model

In this study, we used the Santa Barbara DISORT Atmospheric Radiative Transfer (SBDART) model to calculate spectral surface solar irradiance. Constituting one of the most widely applied models for calculating the atmospheric radiative transfer at Earth's surface, under both clear- and cloudy-sky conditions (Ricchiazzi et al., 1998), SBDART combines a low-resolution atmospheric transmission model, Discrete Ordinate Radiative Transfer (DISORT) module, and Mie scattering output for the scattering of light by ice crystals and water droplets (Stamnes et al., 1988; Fu et al., 2017). Radiative transfer equations for a vertically inhomogeneous, non-isothermal, plane-parallel atmosphere are integrated numerically using the DISORT module. SBDART comprises

multiple standard atmospheric profiles, cloud models, basic surface types, as well as vertical distribution models for aerosols and gas absorption, and enables users to specify these input parameters in real values. In our study, the subarctic and midlatitude winter standard atmospheric condition is performed as well as the tropospheric and stratospheric background aerosols are archived in SBDART (Tanre, D. et al., 1990). According to Dang et al. (2017), the cloud optical depth in high-latitude and mid-latitude was assumed as 11 and 20 under cloudy-sky condition, respectively. The spectral irradiance from SBDART is only used for integrating the spectral MODIS albedo to achieve broadband albedo, thus the uncertainty of solar irradiance from the assumed atmospheric properties has limited influence on the retrieval of radiative forcing (see Section 3.2). Average incident direct and diffuse solar spectra for December-May under clear/cloudy sky are shown in Fig. S1.

The Snow, Ice, and Aerosol Radiative (SNICAR) model is a two-stream multiple scattering radiative transfer model (Flanner et al., 2007, 2009) that has been used widely both to simulate the albedo, transmission, and vertical absorptivity of LAP-contaminated snowpack and to estimate RFLS (Painter et al., 2012a; Bryan et al., 2013; Miller et al., 2016). SNICAR employs the theory proposed by Wiscombe and Warren (1980) and Toon et al. (1989). Specifically, snow is considered to be composed of aggregated ice grains with optical effective radii (R_{eff}) of 50–1500 μm, lognormal distribution, and spherical grain shape. SNICAR also accounts for the incident radiation at the surface and its spectral distribution, solar zenith angle, snow depth and density,

snow layer number, and the type and concentration of LAPs in the snowpack. The model's ability to provide realistic simulations of snow albedo has been verified by several previous studies (Hadley and Kirchstetter, 2012; Meinander et al., 2013; Zhong et al., 2017; Wang et al., 2017).

3.2. Retrieval of quantitative snow properties from remote sensing

The variability of spectral snow albedo depends on the LAP content, grain size, grain shape, and depth of the snowpack, in addition to solar zenith angle. As shown in Fig. 1a, the deposition of BC (as representative of LAPs generally) serves to decrease the albedo of snow significantly, particularly in the ultraviolet (UV) and VIS wavelengths, which account for approximately half of all direct solar irradiance and the majority of diffuse solar irradiance (Fig. S1). In contrast, the impact of BC on albedo is considerably smaller in NIR wavelengths and can be negligible at $>\sim1150$ nm. Snow depth plays a similar role to LAP content and primarily affects albedo in UV and VIS wavelengths (Fig. 1b).

Although snow albedo decreases with snow depth, previous studies have tended to assume a semi-infinite snowpack for which albedo is independent of depth. As a consequence, the role of LAPs in albedo reduction has been overestimated for those areas where the snowpack is thin (Warren, 2013). In this study, we incorporated ERA-Interim SWE data in our SNICAR model simulations to correct for the snow-depth overestimation effect. In contrast, snow grain-size and solar zenith angle influence the snow albedo chiefly in NIR wavelengths (Fig. 1c, d). Specifically, albedo tends to

decrease with increasing snow grain-size and declining solar zenith angle. In this study,

we derived quantitative snow parameters (grain size, albedo reduction, and RFLS) from

MODIS data in conjunction with the SNICAR and SBDART models. The specific

workflow for retrieving RFLS from satellite data is shown in Fig. 2.

3.2.1. Retrieval of blue-sky albedo

MCD43 provides black-sky and white-sky albedo, which are defined as albedo in the

absence of diffuse and direct competent of solar irradiance. Accordingly, the actual

spectral albedo for a land surface at wavelength λ (also called blue-sky albedo:

$\alpha_{MODIS,\lambda}^{blue-clear}$) under clear-sky condition can be calculated as follows:

$$\alpha_{MODIS,\lambda}^{blue-clear} = f_{dif,\lambda}^{clear} \cdot \alpha_{MODIS,\lambda}^{white-sky} + (1 - f_{dif,\lambda}^{clear}) \cdot \alpha_{MODIS,\lambda}^{black-sky} \tag{1}$$

where $\alpha_{MODIS,\lambda}^{white-sky}$ and $\alpha_{MODIS,\lambda}^{black-sky}$ are MODIS-derived values for white-sky and

black-sky albedo, respectively, and $f_{dif,\lambda}^{clear}$ is the ratio of diffuse irradiance to the total

solar irradiance under clear-sky (Lewis and Barnsley, 1994). The latter is calculated as

follows:

$$f_{dif,\lambda}^{clear} = \frac{E_{dif}^{clear}(\lambda; \varphi)}{E_{dif}^{clear}(\lambda; \varphi) + E_{dir}^{clear}(\lambda; \varphi) \cdot cos\beta} \tag{2}$$

where φ is latitude, and $E_{dif}^{clear}(\lambda; \varphi)$ and $E_{dir}^{clear}(\lambda; \varphi)$ denote diffuse and direct

spectral solar irradiance, respectively, derived from the SBDART model under clear-

sky condition. β represents local solar zenith angle, which is obtained using the

topographic correction method (Teillet et al., 1982; Negi and Kokhanovsky, 2011):

$$\cos \beta = \cos \theta_0 \cos \theta_T + \sin \theta_0 \sin \theta_T \cos(\phi_0 - \phi_T) \tag{3}$$

1 for which θ_0 represents the solar zenith angle for a horizontal surface, ϕ_0 is the solar

2 azimuth angle, and θ_T and ϕ_T denote slope inclination and aspect, respectively.

3 Similarly, we can derive the blue-sky albedo for cloudy-sky condition ($\alpha_{MODIS,\lambda}^{blue-cloudy}$).

4 Then, we used cloud fraction (f_{cloud}) from CERES to weight clear-sky albedo and

5 cloudy-sky albedo to obtain actual all-sky albedo ($\alpha_{MODIS,\lambda}^{all}$):

6 $$\alpha_{MODIS,\lambda}^{all} = f_{cloud} \cdot \alpha_{MODIS,\lambda}^{blue-cloudy} + (1 - f_{cloud}) \cdot \alpha_{MODIS,\lambda}^{blue-clear} \qquad (4)$$

7 **3.2.2. Retrieval of snow cover and albedo values**

8 As shown in Fig. 2, the snow-covered area is mapped according to the actual all-sky

9 albedo ($\alpha_{MODIS,\lambda}^{all}$) in band 4 (band center ~555 nm) and the Normalized Difference

10 Snow Index (NDSI), both of which are required to exceed 0.6 (Negi and Kokhanovsky,

11 2011). According to the MODIS Snow Products Collection 6 User Guide

12 (http://nsidc.org/data), the Fractional Snow Cover (FSC) can be calculated as follows:

13 $$FSC = -0.01 + 1.45 \cdot NDSI \qquad (5)$$

14 Accordingly, the identified snow-covered area (ISCA) has an FSC value of >86% but

15 not always 100%. Therefore, the MODIS-derived albedo for a particular ISCA is a

16 combination of values representing both snow and the snow-free underlying surface.

17 Following Pu et al. (2019), the snow albedo ($\alpha_{snow,\lambda}^{all}$) can be distinguished from the

18 mixed albedo by the equation:

19 $$\alpha_{MODIS,\lambda}^{all} = \frac{E_{all-sky,\lambda} \cdot FSC \cdot \alpha_{snow,\lambda}^{all} + E_{all-sky,\lambda} \cdot (1 - FSC) \cdot \alpha_{underlying,\lambda}}{E_{all-sky,\lambda}}$$

$$= FSC \cdot \alpha_{snow,\lambda}^{all} + (1 - FSC) \cdot \alpha_{underlying,\lambda} \qquad (6)$$

$$\alpha_{snow,\lambda}^{all} = \frac{\alpha_{MODIS,\lambda}^{all} - (1 - FSC) \cdot \alpha_{underlying,\lambda}}{FSC} \qquad (7)$$

where $E_{all-sky,\lambda}$ is total solar irradiance under all-sky condition, a linear combination

of direct/diffuse competent of solar irradiance under clear-sky and cloudy-sky using

similar strategy via Eq. (1)-(4). $\alpha_{underlying,\lambda}$ represents the albedo of the underlying

surface and was obtained from Siegmund and Menz (2005). As depicted in Fig. 3b,

vegetation and bare soil are the main types of underlying surface in the ISCA.

3.2.3. Retrieval of snow grain size

The snow optical-equivalent grain size (R_{eff}) is retrieved by fitting SNICAR-simulated

snow albedo to MODIS-derived snow albedo at 1240 nm (the central wavelength of

MODIS band 5), following the protocol of Nolin and Dozier (2000). This retrieval

method is not influenced by liquid water and water vapor and has been employed

widely in previous studies (e.g., Painter et al., 2013; Seidel et al, 2016). Both Nolin and

Dozier (2000) and Pu et al. (2019) reported that the retrieved R_{eff} compares favorably

with ground-based measurements of snow grain size. In this study, we chose to exclude

the ISCA, where MODIS-derived snow albedo at 1240 nm is <0.3, to avoid

misrepresenting R_{eff} (Tedesco et al., 2007).

3.2.4. Retrieval of snow albedo reduction and RFLS

The spectrally integrated reduction in snow albedo due to LAPs ($\Delta\alpha_{MODIS,noon}^{LAPs}$) is

estimated for local-noon and all-sky conditions, using solar irradiance and the

difference between MODIS-derived spectral snow albedo ($\alpha_{snow,\lambda}^{all}$) and simulated pure

snow albedo ($\alpha_{snow,\lambda}^{mdl}$). Because MODIS provides only four VIS bands, we fitted snow

albedo data obtained via MODIS to a continuous 300–2500 nm spectrum ($\alpha_{snow,\lambda}^{MODIS}$, with

a 10 nm interval) following the method provided by Pu et al. (2019). Thereafter, the

broadband albedo reduction due to LAPs retrieved from MODIS ($\Delta\alpha_{MODIS,noon}^{LAPs}$) can

be calculated as follows:

$$\Delta\alpha_{MODIS,noon}^{LAPs} = \frac{\sum_{\lambda=300nm}^{\lambda=2500nm}\left(\alpha_{snow,\lambda}^{mdl} - \alpha_{snow,\lambda}^{MODIS}\right) \cdot E_{all-sky,\lambda} \cdot \Delta\lambda}{\sum_{\lambda=300nm}^{\lambda=2500nm} E_{all-sky,\lambda} \cdot \Delta\lambda} \qquad (8)$$

where $\alpha_{snow,\lambda}^{mdl}$ is the pure snow albedo simulated by SNICAR using MODIS-derived

R_{eff} and ERA-Interim snow depth data, $\alpha_{snow,\lambda}^{MODIS}$ is the continuous snow albedo

derived from MODIS retrievals, and $\Delta\lambda$ is 10 nm.

Following Miller et al. (2016), we assumed that the properties for snow and LAPs

remain invariable throughout the day. Based on calculated $\alpha_{snow,\lambda}^{mdl}$ and $\alpha_{snow,\lambda}^{MODIS}$ at

noon, the diurnal variation of pure and polluted snow albedo can be simulated by

SNICAR from sunrise to sunset. Then, daily-average snow albedo reduction

($\Delta\alpha_{MODIS,daily}^{LAPs}$) can be derived by integrating the diurnal snow albedo reduction, which

is weighted by simultaneous solar irradiance from SBDART. Similarly, we used

measurements of LAPs in contaminated snow to calculate the

in-situ reduction in snow albedo ($\Delta\alpha_{in-situ,daily}^{LAPs}$). To derive a correction factor for

MODIS retrievals, we applied a similar validation strategy to that of Zhu et al. (2017):

$$c = \frac{1}{n}\sum_{i=1}^{n}\left(\frac{\Delta\alpha_{MODIS,daily}^{LAPs}}{\Delta\alpha_{in-situ,daily}^{LAPs}}\right) \qquad (9)$$

where c is the correction factor for $\Delta\alpha_{MODIS,daily}^{LAPs}$ and n is the number of the respective in-situ measurements. Accordingly, the corrected albedo reduction ($\Delta\alpha_{MODIS,corrected}^{LAPs}$) is calculated as follows:

$$\Delta\alpha_{MODIS,corrected}^{LAPs} = \frac{1}{c} \cdot \Delta\alpha_{MODIS,daily}^{LAPs} \tag{10}$$

The daily-average, spectrally integrated RFLS ($RF_{MODIS,daily}^{LAPs}$) is calculated for all-sky conditions as follows:

$$RF_{MODIS,daily}^{LAPs} = \Delta\alpha_{MODIS,corrected}^{LAPs} \cdot SW_{all-sky} \tag{11}$$

where $SW_{all-sky}$ represent the average-daily total downward shortwave fluxes, obtained from CERES under all-sky conditions.

3.2.5. Attribution of spatial variability in snow albedo reductions and radiative forcing

As demonstrated above, reductions in snow albedo and RFLS are dependent primarily on LAP content, R_{eff}, snow depth (SD), solar zenith angle, surface topography, and solar irradiance, the latter three of which can be categorized as the geographic factor (G). We used an impurity index (I_{LAPs}) to represent the LAP content of the snowpack (Di Mauro et al., 2015; Pu et al., 2019), following the equation:

$$I_{LAPs} = \frac{\ln(\alpha_{snow,band4}^{all})}{\ln(\alpha_{snow,band5}^{all})} \tag{12}$$

where $\alpha_{snow,band4}^{all}$ and $\alpha_{snow,band5}^{all}$ are the MODIS-derived snow albedo values for bands 4 and 5, respectively. We then calculated $\Delta\alpha_{MODIS,corrected}^{LAPs}$ as follows:

$$\Delta\alpha_{MODIS,corrected}^{LAPs} = f(I_{LAPs}, R_{eff}, SD, G) \tag{13}$$

The spatial variability in snow albedo reduction due to I_{LAPs} can be expressed as

$$\Delta\alpha_{MODIS,corrected}^{LAPs}(I_{LAPs}) = f(I_{LAPs}, \overline{R_{eff}}, \overline{SD}, \bar{G}) \qquad (14)$$

where $\overline{R_{eff}}, \overline{SD}$, $\bar{G}$ indicate spatial-mean values of R_{eff}, SD, and G, with $\bar{G}$ requiring spatially constant values for the solar zenith angle, surface topography, and solar irradiance parameters. The following three equations were applied in a similar manner:

$$\Delta\alpha_{MODIS,corrected}^{LAPs}(R_{eff}) = f(\overline{I_{LAPs}}, R_{eff}, \overline{SD}, \bar{G}) \qquad (15)$$

$$\Delta\alpha_{MODIS,corrected}^{LAPs}(SD) = f(\overline{I_{LAPs}}, \overline{R_{eff}}, SD, \bar{G}) \qquad (16)$$

$$\Delta\alpha_{MODIS,corrected}^{LAPs}(G) = f(\overline{I_{LAPs}}, \overline{R_{eff}}, \overline{SD}, G) \qquad (17)$$

We then fitted $\Delta\alpha_{MODIS,corrected}^{LAPs}$ through multiple linear regression:

$$\Delta\alpha_{MODIS}^{LAPs,fit} = a \cdot \Delta\alpha_{MODIS,corrected}^{LAPs}(I_{LAPs}) + b\Delta\alpha_{MODIS,corrected}^{LAPs}(R_{eff}) + c \cdot$$

$$\Delta\alpha_{MODIS,corrected}^{LAPs}(SD) + d \cdot \Delta\alpha_{MODIS,corrected}^{LAPs}(G) \qquad (18)$$

where $\Delta\alpha_{MODIS}^{LAPs,fit}$ is the fitted snow albedo reduction and a, b, c, and d denote the regression coefficients. Figure S3a illustrates how $\Delta\alpha_{MODIS}^{LAPs,fit}$ can explain 99% of the variance in $\Delta\alpha_{MODIS,corrected}^{LAPs}$. Therefore, the attribution of spatial variance in $\Delta\alpha_{MODIS,corrected}^{LAPs}$ can be replaced with $\Delta\alpha_{MODIS}^{LAPs,fit}$, enabling Eq. (18) to be written as follows:

$$\Delta\alpha_{MODIS}^{LAPs,fit} - \overline{\Delta\alpha_{MODIS}^{LAPs,fit}} = a \cdot \left(\Delta\alpha_{MODIS,corrected}^{LAPs}(I_{LAPs}) - \right.$$

$$\overline{\Delta\alpha_{MODIS,corrected}^{LAPs}(I_{LAPs})}) + b \cdot \left(\Delta\alpha_{MODIS,corrected}^{LAPs}(R_{eff}) - \right.$$

$$\overline{\Delta\alpha_{MODIS,corrected}^{LAPs}\left(R_{eff}\right)}\right) + c \cdot \left(\Delta\alpha_{MODIS,corrected}^{LAPs}(SD) - $$

$$\overline{\Delta\alpha_{MODIS,corrected}^{LAPs}(SD)}\right) + d \cdot \left(\Delta\alpha_{MODIS,corrected}^{LAPs}(G) - \overline{\Delta\alpha_{MODIS,corrected}^{LAPs}(G)}\right) \quad (19)$$

where $\Delta\alpha_{MODIS}^{LAPs,fit} - \overline{\Delta\alpha_{MODIS}^{LAPs,fit}}$ is the snow albedo reduction anomaly

$(\Delta\alpha_{MODIS,anomaly}^{LAPs,fit})$. Then, Eq. (19) can be written as

$$\Delta\alpha_{MODIS,anomaly}^{LAPs,fit} = a \cdot \Delta\alpha_{MODIS,corrected,anomaly}^{LAPs}(I_{LAPs}) + b \cdot$$

$$\Delta\alpha_{MODIS,corrected,anomaly}^{LAPs}\left(R_{eff}\right) + c \cdot \Delta\alpha_{MODIS,corrected,anomaly}^{LAPs}(SD) + d \cdot$$

$$\Delta\alpha_{MODIS,corrected,anomaly}^{LAPs}(G). \quad (20)$$

According to Huang and Yi (1991) and Pu et al. (2019), the fractional contribution of

LAP content to the variability in snow albedo reduction ($R_{\Delta\alpha}^{LAPs}$) can be calculated as:

$$R_{\Delta\alpha}^{LAPs} = \frac{1}{m}\sum_{j=1}^{m}\frac{\left(a \cdot \Delta\alpha_{MODIS,corrected,anomaly}^{LAPs}(I_{LAPs})_j\right)^2}{K_j} \quad (21)$$

$$K_j = \left(a \cdot \Delta\alpha_{MODIS,corrected,anomaly}^{LAPs}(I_{LAPs})_j\right)^2 + \left(b \cdot\right.$$

$$\Delta\alpha_{MODIS,corrected,anomaly}^{LAPs}\left(R_{eff}\right)_j\right)^2 + \left(c \cdot \Delta\alpha_{MODIS,corrected,anomaly}^{LAPs}(SD)_j\right)^2 +$$

$$\left(d \cdot \Delta\alpha_{MODIS,corrected,anomaly}^{LAPs}(G)_j\right)^2 \quad (22)$$

where m denotes the length of the data set. Values for $R_{\Delta\alpha}^{R_{eff}}$, $R_{\Delta\alpha}^{SD}$, and $R_{\Delta\alpha}^{G}$ can be

derived in the same way. Similarly, we can obtain the fractional contribution for daily

radiative forcing (R_{RF}^{LAPs}, $R_{RF}^{R_{eff}}$, R_{RF}^{SD}, and R_{RF}^{G}).

4. Results

4.1. Study area

Figure 3a depicts the ISCA employed in this study. Most are located in Eurasia, North

America and the Arctic, which are dominated by grassland, shrublands and bare-soil surfaces (Fig. 3b). Several mid–high-latitude regions that typically support a deep snowpack, including southern Russia, western Europe, and eastern US, are not identified by MODIS as ISCA due to the broad distributions of forest in those areas (Fig. 3b). This pattern is supported by Bond et al. (2006), who demonstrated that, under such vegetated conditions, LAPs in snow exert a relatively minor influence on radiative forcing. On the other hand, the snowpack over midlatitude mountains at such a coarse resolution ($0.05° \times 0.05°$) is too low to identify. In addition, midlatitude mountains are characterized as complex terrain, which will lead to high biases in radiative forcing retrieval at the coarse resolution in spite of topographic correction. Therefore, we didn't report the results over midlatitude mountains in this study.

As illustrated in Fig. 3a, ISCA can be separated into four general regions according to geographical distribution and pollution conditions (Fig. S2a, b): northeastern China (NEC), Eurasia (EUA), North America (NA), and the Arctic. The following analysis of snow albedo reduction and RFLS only concerns ISCA and the periods of the results are mainly in winter for midlatitudes due to snow melting and in spring for the Arctic due to polar night.

4.2. Global characteristics

Previous studies have highlighted the dominant role of BC in light absorption by snow (Wang et al., 2013b; Dang et al., 2017). The spatial distribution of BC emissions density for the Northern Hemisphere in December-May is shown in Fig. S2a. Emissions density

1   exhibits a strong spatial inhomogeneity, ranging from $<10^{-1}$ to $>10^4$ g km^{-2} month^{-1}

2   over ISCA. The highest values occur in NEC, where is considerably higher than EUA

3   and NA, and the lowest values occur in the Arctic. The wet and dry deposition of BC

4   constitute the primary mechanisms for BC accumulation in snow. As shown in Fig. S2b,

5   the distribution of BC deposition (i.e., the sum of dry and wet deposition) is similar to

6   BC emissions density, with the highest and lowest regional averages corresponding to

7   NEC and the Arctic, respectively. Together, these data indicate that the NEC snowpack

8   is heavily polluted, and thus snow albedo reduction is likely to be highest, while the

9   Arctic snowpack is the least contaminated.

10   In addition to LAP content, the physical properties of the snowpack, such as depth and

11   grain size, also impact snow albedo (Fig. 1). As depicted in Fig. 4a, the average

12   snowpack in EUA (0.15 m thick) is thinner than in both NA (0.24 m) and NEC (0.19

13   m), implying a greater impact of snow depth on snow albedo and radiative forcing in

14   EUA. The greatest snow depths occur in the Arctic (>1 m) and can be considered semi-

15   infinite, meaning that the impact of depth on albedo and radiative forcing is negligible.

16   Figure 4b shows the spatial distribution of MODIS-derived snow grain radius (R_{eff}).

17   In contrast to BC emissions density, BC deposition, and snow depth, R_{eff} exhibits

18   minor spatial variability, with regional average values for NEC, EUA, NA, and the

19   Arctic of 237 μm, 227 μm, 237 μm, and 215 μm, respectably. These values align with

20   the findings of several previous studies (Painter et al., 2013; Seidel et al, 2016; Pu et

21   al., 2019) and imply that the contribution of R_{eff} to spatial variability in snow albedo

1   reduction and radiative forcing is negligible.

2   According to Eq. (11), local solar radiances is an important factor for determining RFLS.

3   Figure 4c depicts the December-May averaged total downward surface shortwave flux

4   under all-sky conditions. Average solar radiances flux values for EUA and NA are

5   comparable to one another but high relative to NEC, which lies at a generally higher

6   latitude (>40°). The lowest values occur in the Arctic due to that region's extreme

7   latitude. The Arctic goes through the polar night during winter, so that the radiative

8   effect of LAPs in the Arctic mainly appears in spring. Figure S2d shows the March-

9   May averaged downward surface shortwave flux. As can be seen that the values in the

10   Arctic in March-May are higher than those in midlatitudes in December-February

11   (Figure S2c). We note that snow albedo reduction and radiative forcing are only

12   calculated over the period when snow-covered area was mapped, which implies that the

13   RFLS will be higher in the Arctic than midlatitudes for the same snow albedo reduction.

14   **4.3. Corrections based on in-situ observations**

15   Albedo reduction calculated using in-situ observed LAPs ($\Delta\alpha_{in-situ,daily}^{LAPs}$) were used to

16   quantitatively correct MODIS retrievals through comparison with MODIS-retrieved

17   snow albedo reduction ($\Delta\alpha_{MODIS,daily}^{LAPs}$). Figure S4 displays scatterplots of the ratios of

18   $\Delta\alpha_{MODIS,daily}^{LAPs}$ to $\Delta\alpha_{in-situ,daily}^{LAPs}$ ($r_{in-situ}^{MODIS}$) for each sampling sites (Ye et al., 2012;

19   Wang et al., 2013b, 2017; Doherty et al., 2010; 2014). Briefly, for NA, EUA, and the

20   Arctic where the snowpack is relatively clean, the values for $r_{in-situ}^{MODIS}$ mostly range

21   between 2 and 10. In contrast, the heavily polluted snowpack in NEC returns $r_{in-situ}^{MODIS}$

1 values ranging from 0.5 to 2.5, indicating a negative correlation between the biases of

2 $\Delta\alpha_{MODIS,daily}^{LAPs}$ and snow contamination, and thus supporting the findings of previous

3 studies (Painter et al., 2012a; Pu et al., 2019). To improve the quality of MODIS

4 retrievals, we developed the correction factors for different regions. According to Eq.

5 (10), the correction factors for NEC, EUA, NA, Canadian Arctic, Russian Arctic and

6 Greenland are 1.6, 4.1, 4.1, 4.4, 5.4 and 6.0, respectively. Hereafter, our analyses are

7 based on the corrected MODIS retrievals.

8 Figure 5 compares the corrected MODIS retrievals to measurement-based results, and

9 the mean absolute error (MAE) and root mean square error (RMSE) of

10 $\Delta\alpha_{MODIS,corrected}^{LAPs}$ relative to $\Delta\alpha_{in-situ,daily}^{LAPs}$ are given in Table S1. Together, these

11 results imply that the corrected MODIS retrievals are plausible. Nevertheless, we note

12 that the correction used in this study is spatially rough due to the low density of in-situ

13 measurements, thus that both the uncertainty and bias are non-negligible. To address

14 this issue, we presented further discussion about the accuracy of radiative forcing

15 retrievals (see Sect. 4.5). We also conducted a comprehensive series of comparisons

16 between the MODIS-derived retrievals and values provided via surface measurements,

17 model simulations, and remote sensing (see Sect. 5). We concluded that further field-

18 based measurements of snow albedo are required to improve the quality of satellite

19 retrievals.

20 **4.4. Spatial distributions of snow albedo reduction and radiative forcing**

21 Figure 6a shows the spatial distributions of MODIS-based albedo reduction and daily

radiative forcing, and statistics are shown in Figure 6b and Table 1. On average, $\Delta\alpha_{MODIS,corrected}^{LAPs}$, and $RF_{MODIS,daily}^{LAPs}$ provide respective values of 0.021 and 2.9 W m^{-2} for Northern Hemisphere ISCA. The highest $\Delta\alpha_{MODIS,corrected}^{LAPs}$ occurs in NEC, where the regional average of ~0.11 exceeds those of EUA (~0.031) and NA (~0.027) by a factor of ~3-4. This feature reflects the relatively high rate of emissions over NEC, which results in the highest level of BC deposition over ISCA (Fig. S2a, b). In contrast, being located far from major sources of pollution, the relatively clean Arctic snowpack returns the lowest $\Delta\alpha_{MODIS,corrected}^{LAPs}$ (~0.016) of the entire Northern Hemisphere. Consistent with snow albedo reduction, the highest regional-average daily radiative forcing ($RF_{MODIS,daily}^{LAPs}$) occurs in NEC, with values of ~12 W m^{-2}, and the lowest regional average occurs in the Arctic, with values of ~2.6 W m^{-2}. Regional-average radiative forcing for NA and EUA are both intermediate, with values of ~3.1 W m^{-2} and ~3.5 W m^{-2}, respectively.

On a regional level, NEC $\Delta\alpha_{MODIS,corrected}^{LAPs}$ falls primarily within the range ~0.077–0.14, and intra-regional variability is relatively small due to pervasive heavy pollution (Fig. S2). Compared to snow albedo reduction, the radiative forcing for NEC exhibits a slightly greater spatial variability due to latitude-dependent differences in the flux of surface solar radiances, ranging from ~7.2 W m^{-2} to ~17 W m^{-2}. In NA, where the principal ISCA are located in southern Canada, the western US, and Central America Plains, $\Delta\alpha_{MODIS,corrected}^{LAPs}$ and $RF_{MODIS,daily}^{LAPs}$ tend to range between ~0.014-0.046 and ~1.3-7.0 W m^{-2}, respectively. In EUA, $\Delta\alpha_{MODIS,corrected}^{LAPs}$ and $RF_{MODIS,daily}^{LAPs}$ fall

largely within the respective ranges of ~0.017–0.049 and ~1.6–8.4 W m^{-2}. Central Asia and Mongolia exhibit relatively high values for $\Delta\alpha_{MODIS,corrected}^{LAPs}$ (>0.04) and $RF_{MODIS,daily}^{LAPs}$ (>2 W m^{-2}), while this pattern likely reflects the influence of anthropogenic BC in addition to natural dust (Pu et al., 2017; Zhou et al., 2019) (Fig. S2a–b).

In the Arctic, $\Delta\alpha_{MODIS,corrected}^{LAPs}$ and $RF_{MODIS,daily}^{LAPs}$ both present quite large intra-regional variabilities from ~0.0028 to ~0.046 and ~0.48 to 6.6 W m^{-2}. Greenland has the cleanest snow with $\Delta\alpha_{MODIS,corrected}^{LAPs}$ and $RF_{MODIS,daily}^{LAPs}$ of ~0.011-0.023 and ~0.40-3.3 W m^{-2}. In Canadian Arctic, $\Delta\alpha_{MODIS,corrected}^{LAPs}$ and $RF_{MODIS,daily}^{LAPs}$ are mainly in a range of ~0.012-0.055 and ~0.59-6.1 W m^{-2}. In addition, the relatively high values are found around the edge of ISCA over west of Canadian Arctic. The possible reason is that these areas are suffering from faster snow melting compared with rest of Canadian Arctic in spring, which is characterized by higher snow grain size (Fig. 4b). Hence, more LAPs are accumulated in the surface snow resulting in higher snow albedo reduction. In Russian Arctic, $\Delta\alpha_{MODIS,corrected}^{LAPs}$ and $RF_{MODIS,daily}^{LAPs}$ present a significant altitude-dependent trend of ~0.012-0.048 and ~1.0-7.3 W m^{-2}. The snow albedo reduction in eastern Siberia are quite high and comparable with the values in midlatitudes. Moreover, benefiting from the higher solar radiances in eastern Siberia in Spring (Fig. S2d) than that in midlatitudes in Winter-Spring (Fig. 4c and Fig. S2c), $RF_{MODIS,daily}^{LAPs}$ in eastern Siberia is higher than parts of midlatitudes. Even different from the findings in previous modeling studies (e.g. Flanner et al., 2007; 2009), the

1   results seem to be comparable with the limited ground-based estimates (Fig. S3). The

2   serious biomass burning in eastern Siberia in Spring may be responsible for such high

3   values (Warneke et al., 2010; Hegg et al., 2009). Overall, the Arctic spatial pattern of

4    $\Delta\alpha_{MODIS,corrected}^{LAPs}$ and $RF_{MODIS,daily}^{LAPs}$ in our study is consistent with the previous

5   studies based on field experiments (Dang et al., 2017) and model simulation (Flanner

6   et al., 2007). Nevertheless, we note that readers should be cautious about our reported

7   high values in Russian Arctic and more field experiments are necessary for validating

8   the results.

9   As mentioned above, the assumption of semi-infinite snowpack will trigger an

10   overestimate for radiative forcing when snow depth is not thick enough. Figure 7 shows

11   the spatial distribution of the ratio of retrieved radiative forcing using semi-infinite

12   snow to radiative forcing using ERA-Interim snow depth. As can be seen that semi-

13   infinite snowpack assumption will lead to an overestimate of up to ~25% in midlatitude

14   areas, where snow depth is thin. In contrast, the influence of snow depth on radiative

15   forcing is negligible in the Arctic, where snow is thick enough to become semi-infinite

16   snowpack. These results demonstrated the important impact of snow depth on radiative

17   forcing retrievals, which must be considered to reduce the overestimate for the

18   following study.

19   **4.5. Accuracy discussion**

20   In spite of the rigorous processes for radiative forcing retrieval, the uncertainty is still

21   existed. For example, light-absorbing particles in the atmosphere will reduce the

accuracy of MODIS surface reflectance retrieval, even though the atmospheric

correction has been conducted. In addition, previous study pointed out a high scatter

when converting NDSI to FSC using Eq. (5), which will induce bias in snow albedo

retrieval (Rittger et al., 2013; Riggs et al., 2016). Furthermore, the method for snow

grain size retrieval is only based on a single MODIS band at 1.24 μm, which could lead

to higher uncertainties. Above all, all of these factors will result in a non-negligible

uncertainty for radiative forcing retrieval, which needs to be further discussed.

To account for this issue, we consider that the accuracy of atmospheric correction is

typically ± (0.005 + 0.05*reflectance) under conditions that AOD is less than 5.0 and

solar zenith angle is less than 75° according to the MODIS Surface Reflectance User's

Guide (Collection 6, https://modis.gsfc.nasa.gov/data/dataprod/mod09.php). In

addition, the bias for FSC calculation is assumed as 10% according to Riggs et al.

(2016). The bias for snow grain size retrieval is assumed as 30% according to the studies

of Pu et al. (2019) and Wang et al. (2017). Figure 8 shows the overall uncertainty of

radiative forcing retrieval due to all these factors while Figure S6 show the uncertainty

caused by each factor. In general, the positive (negative) uncertainty falls in a range of

15%~108% (-106%~-20%), with atmospheric correction and FSC calculation by higher

uncertainties than snow grains size retrieval. The highest uncertainty occurs in the

Arctic while the lowest uncertainty occurs in NEC. Furthermore, the uncertainty shows

a negative correlation with retrieved radiative forcing. The results indirectly

demonstrated the reasonability of different correction factors performed in different

1   regions. For example, the value of 1.6 used in NEC suggests that the correction

2   approach works well for heavily polluted snow, while the value of 6.0 used in Greenland

3   for relatively clean snow suggests that the method becomes not accurate enough.

4   It worth noting that the uncertainties from these factors could not fully explain the high

5   correction factor in clean snow. There are four probable reasons: (1) the rough snow

6   surface and uncertainties of vegetation and soil reflectance can effectively influence

7   radiative forcing retrieval; (2) MODIS cannot proceed with a continuous spectral

8   measurement of a continuous variable forcing like what LAPs afford to snow albedo

9   due to the variably spaced and discrete bands of MODIS, which prevents a more

10   quantitative retrieval and thus results in a non-negligible uncertainty in radiative forcing

11   retrieval (Painter et al., 2012); (3) We use the retrieved radiative forcing in a pixel size

12   of 0.05° × 0.05° to compare with the in-situ radiative forcing calculated from the

13   measured BC_{equiv} concentration with the sample site located in the center of the pixel.

14   However, such a comparison may not be true at some sites due to the inhomogeneous

15   spatial distribution of LAP contents, which will influence radiative forcing retrieval; (4)

16   In-situ measurements also have uncertainties, which may cause a high bias for snow

17   albedo reduction in clean snow. For example, a 10% bias for 50 ng g^{-1} BC can result in

18   an 8% bias for snow albedo reduction.

19   **4.6. Attribution to the spatial variability of snow albedo reduction and radiative**

20   **forcing**

21   Here, we address the attributions to the spatial variability of snow albedo reduction and

radiative forcing. As discussed in Sect. 3.2.5, the spatial variability in snow albedo

reduction and radiative forcing are largely dependent on LAP content, snow grain radius,

snow depth, and the geographic factor. Figure 9 illustrates the fractional contributions

of each factor within the study regions. For the Northern Hemisphere ISCA as a whole,

LAPs (I_{LAPs}) is the greatest contributor (84.3%) to snow albedo reduction, followed by

SD (13.7%); R_{eff} and G have only a minor influence (1.9% and <1%, respectively)

(Fig. 9a). This result confirms that the concentration of LAPs in the snowpack plays a

fundamental role in spatial variability of snow albedo reduction.

LAPs also constitute the dominant contributors to snow albedo reduction on a regional

scale, accounting for 96.0% of the Arctic signal and 56.7% in EUA and 49.9% in NA,

and are the second largest contributor in NEC (40.3%). The contribution of SD is

greatest in NEC (56.3%), with slightly lower values in EUA (40.3%) and NA (48.8%),

reflecting the significant spatial variability in SD across these regions. In the Arctic,

the snowpack is sufficiently thick to be considered a homogeneous, semi-infinite

snowpack and thus the contribution of SD is negligible. In contrast, R_{eff} makes only

minor contributions in NEC (3.3%), NA (1.3%), EUA (2.8%) and the Arctic (1.4%).

Finally, G makes the smallest contribution to snow albedo reduction (<1%), both on

regional and global scales.

On a hemispheric scale, the greatest contributors to radiative forcing are LAP content

(70.0%) and G (22.3%), followed by SD (7.6%). As with snow albedo reduction,

R_{eff} plays only a minor role. The influence of G on spatial variability in radiative

forcing is attributed to the high degree of variability in latitude-dependent solar

radiances among ISCA. On a regional scale, the respective contributions of LAP

content, G, and SD are also comparable among the four study areas, accounting for

34.1%, 11.1%, and 52.0% of radiative forcing in NEC, 39.2%, 13.9%, and 46.4% in

NA, and 48.0%, 19.3%, and 31.6% in EUA. The Arctic radiative forcing is dominated

by LAPs (85.6%) and G (12.7%).

In summary, LAPs play a dominant role in the spatial variability of snow albedo

reduction and radiative forcing. Our results also highlight the significant contribution

of SD to snow albedo reduction and G to radiative forcing.

4.7. Comparisons with model simulations

To investigate the global distribution and variance of RFLS, previous studies have

tended to rely on Earth system models with minimal cross-checking from in-situ

measurements or remote sensing observations (Qian et al., 2015; Skiles et al., 2018). In

this study, we compared MODIS retrievals with CESM2 to improve our understanding

of the magnitude of RFLS on a global scale.

Employing snow BC concentrations from CESM2, we also calculated December-May

daily radiative forcing (RF_{CESM2}) for the Northern Hemisphere ISCA during the period

2003–2014 (Fig. 10a). Statistics are presented in Fig. S7. Briefly, RF_{CESM2} exhibits

strong spatial inhomogeneity, with values ranging from 0.20 W m^{-2} to 5.6 W m^{-2}. The

highest regional average in RF_{CESM2} occurs in NEC ($\geq$10 W m^{-2}) and the lowest in

the Arctic ($\leq$0.5 W m^{-2}), consistent with $RF^{LAPs}_{MODIS,daily}$.

Figure 10b depicts the comparison of $RF^{LAPs}_{MODIS,daily}$ and RF_{CESM2}. In NEC, RF_{CESM2} (15 W m^{-2}) compares well with $RF^{LAPs}_{MODIS,daily}$ (12 W m^{-2}), with a significant correlation at the 99% confidence level. For EUA, RF_{CESM2} (3.8 W m^{-2}) is similar to $RF^{LAPs}_{MODIS,daily}$ (3.5 W m^{-2}). For NA, RF_{CESM2} (1.2 W m^{-2}) is lower than $RF^{LAPs}_{MODIS,daily}$ (3.1 W m^{-2}) and the spatial correlation between them are poor. In the Arctic, RF_{CESM2} is correlated with $RF^{LAPs}_{MODIS,daily}$ at the 99% confidence level. However, RF_{CESM2} (1.7 W m^{-2}) is lower than $RF^{LAPs}_{MODIS,daily}$ (2.6 W m^{-2}) by a factor of 1.5.

Overall, the RFLS derived from our MODIS retrievals and modeling-based estimates exhibit a same magnitude over the Northern Hemisphere. In NEC, the MODIS- derived and model-derived estimates show good general agreement, indicating the satisfactory performance of Earth system modeling in this heavily polluted region. In EUA, average radiative forcing values are comparable but the spatial correlation is relatively poor, while MODIS retrievals for the Arctic are significantly higher than those simulations.

5. Discussion

In recent decades, there has been increasing scientific interest in snow LAPs due to their role in the climate system, and numerous studies have attempted to evaluate RFLS. In addition to making global-scale comparisons between our MODIS retrievals and model-based estimates, this study collects a comprehensive set of radiative forcing

estimates, based on local-scale observations and remote sensing, to make quantitative regional- and global-scale comparisons and synthetically evaluate the magnitude of RFLS (Table 2). This approach also affords the opportunity to examine the MODIS retrievals used in our study.

Dang et al. (2017) reported RFLS values of 7–18 W m^{-2}, 0.6–1.9 W m^{-2}, and 0.1–0.8 W m^{-2} for northern China, North America, and the Arctic, respectively, which only focused on the period of January-March, and therefore are smaller than our retrievals. In NA, Sterle et al. (2013) estimated a daily-averaged RFLS of ~2.5-40 W m^{-2} for the eastern Sierra Nevada in February-May, 2009, while Miller et al. (2016) reported a daily RFLS of ~35-86 (37-100) W m^{-2} based on in-situ measurements (remote sensing) in the San Juan Mountains in May 2010. Both values are higher than our estimate (~3.1 W m^{-2}), potentially due to the significant dust deposition in those areas.

We also collected the average-daily RFLS simulated by regional and/or global climate models (Table 2). For NEC, Zhao et al. (2014) and Qian et al. (2014) reported values of 10 W m^{-2} in January-February and 5–10 W m^{-2} in April, respectively. In NA, Qian et al. (2009) provided an estimate of 3–7 W m^{-2} for the central Rockies and southern Alberta in March, while Oaida et al. (2015) reported an average RFLS of 16 W m^{-2} over the western US in spring. Finally, Qian et al. (2014) and Qi et al. (2017) estimated RFLS values of <0.3 W m^{-2} and 0.024–0.39 W m^{-2} for the Arctic in April, respectively. We consider our retrievals for NEC to be comparable with these regional model simulations, despite some disparity. However, we note that our result is significantly

lower than those of previous studies in NA, but higher in the Arctic.

On a global scale, Hansen and Nazarenko (2004) reported the RFLS is 0.3 W m^{-2}, while Flanner et al. (2007) showed a RFLS of ~0.05 W m^{-2}. For the North Hemisphere as a whole, Bond et al. (2013) estimated a climate forcing of 0.13 W m^{-2}. Each of these previous values is significantly lower than our retrieval (~2.9 W m^{-2}). However, those studies included all areas regardless of snow covered throughout the whole year, while our results are only for Northern Hemisphere ISCA from December to May.

Overall, we consider our MODIS-based retrievals to be physical realistic on both regional and global scales, although we note a number of differences between our results and those generated by different methods. On the other hand, while in-situ measurements are the most precise, their spatial coverage is restricted by logistical limitations and the extreme environments involved. Conversely, models can provide broad perspectives of climatic impacts yet are typically undermined by large uncertainty. Therefore, we argue that remote sensing provides a powerful technique, with high spatial and temporal resolutions, that can bridge the gap between in-situ measurements and climate models and reduce the uncertainties associated with the latter. Further retrieval of remote-sensing data, including the use of multiple satellites and sensors, is therefore warranted to exploit this opportunity fully. We also indicate the fact that parts of central EUA and Russian Arctic, however, studies are barely performed but desired. Finally, we note that in-situ observations remain limited, and more field campaigns are needed to constrain remote sensing retrievals and modeling simulations.

6. Conclusion

We presented a global-scale evaluation of the daily radiative forcing of LAPs in the Northern Hemisphere snowpack (RFLS), estimated from remote-sensing data. The satellite-retrieved RFLS also has implications for expanding the value of limited in-situ measurements, which can provide valuable information for climate models and help optimize model simulations.

Based on the corrected snow albedo reduction ($\Delta\alpha_{MODIS,corrected}^{LAPs}$), we calculated average-daily RFLS ($RF_{MODIS,daily}^{LAPs}$) during December-May for the period 2003–2018. For the identified snow covered area over Northern Hemisphere as a whole, average $\Delta\alpha_{MODIS,corrected}^{LAPs}$ is ~0.021 and $RF_{MODIS,daily}^{LAPs}$ is ~2.9 W m^{-2}. We also observed distinct spatial variability in snow albedo reduction and RFLS. The highest regional-average $\Delta\alpha_{MODIS,corrected}^{LAPs}$ (~0.11) and $RF_{MODIS,daily}^{LAPs}$ (~12 W m^{-2}) occur in northeastern China, while the lowest regional averages of ~0.016 and ~2.6 W m^{-2}, respectively, are observed in the Arctic. Moreover, we indicated that the semi-infinite assumption could overestimates up to ~25% of RFLS, especially for thin and patchy snow, such as midlatitudes in Eurasia and NA. In addition, if the ground-based corrections were not considered, the total uncertainty of RFLS retrievals is in the range of 15%~108% (-106%~-20%) due to atmospheric correction, snow cover fraction calculation and snow grain size retrieval.

Following this assessment, we made quantitative attributions of the spatial variability in snow albedo reduction and radiative forcing. Our results indicate that the LAP

content is the largest contributor (84.3%) to spatial variance in snow albedo reduction, followed by snow depth (13.7%), whereas snow grain size (1.9%) and the geographic factor G (<1%) are only minor contributors on a Northern Hemispheric scale. LAP content and G account for 70.0% and 22.3% of the spatial variability of radiative forcing, respectively, following by SD (7.6%) over Northern Hemisphere.

Retrieved RFLS values are compared spatially with the model-derived estimates of the CESM2. Our results indicate that MODIS retrievals show the same magnitude with modeled estimates for Northern Hemisphere. However, although the Earth system models perform well in NEC, there remain large uncertainties in the Arctic. To evaluate and examine the MODIS retrievals synthetically, we then compared the retrieved RFLS to previously published estimates, including local-scale observations, remote sensing retrievals, and regional- and global-scale model simulations. The results of this evaluation suggest that MODIS retrievals are generally realistic, despite a number of important differences among the various methods.

Finally, we urge the community to expand the ground-based measurements of the global snowpack, particularly in those regions currently lacking in-situ observations. Such development would help further constrain and improve satellite-based retrievals in the future. We propose that climate models validated by these refined remote sensing retrievals should be able to capture the RFLS more accurately, thereby providing more reliable estimates of the future impacts of global climate change.

Data availability.

MODIS data can be found at https://earthdata.nasa.gov/ (last access: 20 January 2019).

CERES data can be found from NASA's Clouds and the Earth's Radiant Energy System at https://ceres.larc.nasa.gov (last access: 12 April 2019). Shuttle Radar Topography Mission (SRTM) digital elevation data are provided by the US Geological Survey at https://www.usgs.gov/ (last access: 9 December 2018). Snow depth can be found from ERA-Interim at https://www.ecmwf.int (last access: 15 January 2019). BC emission data can be found at http://inventory.pku.edu.cn (last access: 5 June 2019). BC deposition data can be found at https://gmao.gsfc.nasa.gov/reanalysis/MERRA-2/ (last access: 5 June 2019). CMIP6 data can be found at https://esgf-node.llnl.gov/ (last access: 15 July 2019). Surface measurement datasets are from Wang et al. (2013, 2017), Ye et al. (2012) and Doherty et al. (2010, 2014). Springtime radiative forcing due to LAPs in snow is derived from a GCM run by Flanner et al. (2007).

1 **Author contributions.**

2 PW and WX designed the study and evolved the overarching research goals and aims.

3 CJC carried the study out and wrote the first draft with contributions from all co-authors.

4 CJC and STL applied formal techniques such as statistical, mathematical and

5 computational to analyze study data. ZY prepared input data and managed activities to

6 annotate, scrub data and maintain research data. WDY completed the implementation

7 of the computer code and supporting algorithms used for the calculations in this study.

8 PW and WX assumed oversight and leadership responsibility for the research activity

9 planning and execution. All authors contributed to the improvement of results and

10 revised the final paper.

1 **Competing interests.**

2 The authors declare that they have no conflict of interest.

3 **Acknowledgments**

4 This research was supported jointly by the National Key R&D Program of China

5 (2019YFA0606801), the National Natural Science Foundation of China (grants

6 41975157, 41775144, and 41875091), the China Postdoctoral Science Foundation

7 (2020M673530).

References

Bair, E. H., Rittger, K., Skiles, S. M., and Dozier, J.: An Examination of Snow Albedo Estimates From MODIS and Their Impact on Snow Water Equivalent Reconstruction, Water Resources Research, 10.1029/2019wr024810, 2019.

Barnett, T. P., Adam, J. C., and Lettenmaier, D. P.: Potential impacts of a warming climate on water availability in snow-dominated regions, Nature, 438, 303-309, 10.1038/nature04141, 2005.

Berrisford, P., Kållberg, P., Kobayashi, S., Dee, D., Uppala, S., Simmons, A. J., Poli, P., and Sato, H.: Atmospheric conservation properties in ERA-Interim, Quarterly Journal of the Royal Meteorological Society, 137, 1381-1399, 10.1002/qj.864, 2011.

Bian, H., Colarco, P. R., Chin, M., Chen, G., Rodriguez, J. M., Liang, Q., Blake, D., Chu, D. A., da Silva, A., Darmenov, A. S., Diskin, G., Fuelberg, H. E., Huey, G., Kondo, Y., Nielsen, J. E., Pan, X., and Wisthaler, A.: Source attributions of pollution to the Western Arctic during the NASA ARCTAS field campaign, Atmospheric Chemistry and Physics, 13, 4707-4721, 10.5194/acp-13-4707-2013, 2013.

Bond, T. C., Habib, G., and Bergstrom, R. W.: Limitations in the enhancement of visible light absorption due to mixing state, Journal of Geophysical Research, 111, 10.1029/2006jd007315, 2006.

Bond, T. C., Doherty, S. J., Fahey, D. W., Forster, P. M., Berntsen, T., DeAngelo, B. J., Flanner, M. G., Ghan, S., Kärcher, B., Koch, D., Kinne, S., Kondo, Y., Quinn, P. K.,

Sarofim, M. C., Schultz, M. G., Schulz, M., Venkataraman, C., Zhang, H., Zhang, S., Bellouin, N., Guttikunda, S. K., Hopke, P. K., Jacobson, M. Z., Kaiser, J. W., Klimont, Z., Lohmann, U., Schwarz, J. P., Shindell, D., Storelvmo, T., Warren, S. G., and Zender, C. S.: Bounding the role of black carbon in the climate system: A scientific assessment, Journal of Geophysical Research: Atmospheres, 118, 5380-5552, 10.1002/jgrd.50171, 2013.

Brandt, R. E., Warren, S. G., and Clarke, A. D.: A controlled snowmaking experiment testing the relation between black carbon content and reduction of snow albedo, Journal of Geophysical Research, 116, 10.1029/2010jd015330, 2011.

Brown, R. D., and Mote, P. W.: The Response of Northern Hemisphere Snow Cover to a Changing Climate, Journal of Climate, 22, 2124-2145, 10.1175/2008jcli2665.1, 2009.

Brun, E., Vionnet, V., Boone, A., Decharme, B., Peings, Y., Valette, R., Karbou, F., and Morin, S.: Simulation of Northern Eurasian Local Snow Depth, Mass, and Density Using a Detailed Snowpack Model and Meteorological Reanalyses, Journal of Hydrometeorology, 14, 203-219, 10.1175/jhm-d-12-012.1, 2013.

Bryant, A. C., Painter, T. H., Deems, J. S., and Bender, S. M.: Impact of dust radiative forcing in snow on accuracy of operational runoff prediction in the Upper Colorado River Basin, Geophysical Research Letters, 40, 3945-3949, 10.1002/grl.50773, 2013.

Chin, M., Ginoux, P., Kinne, S., Torres, O., Holben, B. N., Duncan, B. N., Martin, R. V., Logan, J. A., Higurashi, A., and Nakajima, T.: Tropospheric Aerosol Optical

Thickness from the GOCART Model and Comparisons with Satellite and Sun Photometer Measurements, Journal of the Atmospheric Sciences, 59, 461-483, 10.1175/1520-0469(2002)059<0461:taotft>2.0.co;2, 2002.

Colarco, P., da Silva, A., Chin, M., and Diehl, T.: Online simulations of global aerosol distributions in the NASA GEOS-4 model and comparisons to satellite and ground-based aerosol optical depth, Journal of Geophysical Research, 115, 10.1029/2009jd012820, 2010.

Colombo, R., Garzonio, R., Di Mauro, B., Dumont, M., Tuzet, F., Cogliati, S., Pozzi, G., Maltese, A., and Cremonese, E.: Introducing Thermal Inertia for Monitoring Snowmelt Processes With Remote Sensing, Geophysical Research Letters, 46, 4308-4319, 10.1029/2019gl082193, 2019.

Danabasoglu, G., Lamarque, J. F., Bacmeister, J., Bailey, D. A., DuVivier, A. K., Edwards, J., Emmons, L. K., Fasullo, J., Garcia, R., Gettelman, A., Hannay, C., Holland, M. M., Large, W. G., Lauritzen, P. H., Lawrence, D. M., Lenaerts, J. T. M., Lindsay, K., Lipscomb, W. H., Mills, M. J., Neale, R., Oleson, K. W., Otto-Bliesner, B., Phillips, A. S., Sacks, W., Tilmes, S., Kampenhout, L., Vertenstein, M., Bertini, A., Dennis, J., Deser, C., Fischer, C., Fox-Kemper, B., Kay, J. E., Kinnison, D., Kushner, P. J., Larson, V. E., Long, M. C., Mickelson, S., Moore, J. K., Nienhouse, E., Polvani, L., Rasch, P. J., and Strand, W. G.: The Community Earth System Model Version 2 (CESM2), Journal of Advances in Modeling Earth Systems, 12, 10.1029/2019ms001916, 2020.

1 Dang, C., Brandt, R. E., and Warren, S. G.: Parameterizations for narrowband and

2 broadband albedo of pure snow and snow containing mineral dust and black carbon,

3 Journal of Geophysical Research: Atmospheres, 120, 5446-5468,

4 10.1002/2014jd022646, 2015.

5 Dang, C., Warren, S. G., Fu, Q., Doherty, S. J., Sturm, M., and Su, J.: Measurements of

6 light-absorbing particles in snow across the Arctic, North America, and China: Effects

7 on surface albedo, J Geophys Res-Atmos, 122, 10149-10168, 2017.

8 Dee, D. P., Uppala, S. M., Simmons, A. J., Berrisford, P., Poli, P., Kobayashi, S., Andrae,

9 U., Balmaseda, M. A., Balsamo, G., Bauer, P., Bechtold, P., Beljaars, A. C. M., van de

10 Berg, L., Bidlot, J., Bormann, N., Delsol, C., Dragani, R., Fuentes, M., Geer, A. J.,

11 Haimberger, L., Healy, S. B., Hersbach, H., Hólm, E. V., Isaksen, L., Kållberg, P.,

12 Köhler, M., Matricardi, M., McNally, A. P., Monge-Sanz, B. M., Morcrette, J. J., Park,

13 B. K., Peubey, C., de Rosnay, P., Tavolato, C., Thépaut, J. N., and Vitart, F.: The ERA-

14 Interim reanalysis: configuration and performance of the data assimilation system,

15 Quarterly Journal of the Royal Meteorological Society, 137, 553-597, 10.1002/qj.828,

16 2011.

17 Deems, J. S., Painter, T. H., Barsugli, J. J., Belnap, J., and Udall, B.: Combined impacts

18 of current and future dust deposition and regional warming on Colorado River Basin

19 snow dynamics and hydrology, Hydrology and Earth System Sciences, 17, 4401-4413,

20 10.5194/hess-17-4401-2013, 2013.

1   Di Mauro, B., Fava, F., Ferrero, L., Garzonio, R., Baccolo, G., Delmonte, B., and

2   Colombo, R.: Mineral dust impact on snow radiative properties in the European Alps

3   combining ground, UAV, and satellite observations, Journal of Geophysical Research:

4   Atmospheres, 120, 6080-6097, 10.1002/2015jd023287, 2015.

5   Di Mauro, B., Baccolo, G., Garzonio, R., Giardino, C., Massabò, D., Piazzalunga, A.,

6   Rossini, M., and Colombo, R.: Impact of impurities and cryoconite on the optical

7   properties of the Morteratsch Glacier (Swiss Alps), The Cryosphere, 11, 2393-2409,

8   10.5194/tc-11-2393-2017, 2017.

9   Di Mauro, B., Garzonio, R., Rossini, M., Filippa, G., Pogliotti, P., Galvagno, M., Morra

10 di Cella, U., Migliavacca, M., Baccolo, G., Clemenza, M., Delmonte, B., Maggi, V.,

11 Dumont, M., Tuzet, F., Lafaysse, M., Morin, S., Cremonese, E., and Colombo, R.:

12 Saharan dust events in the European Alps: role in snowmelt and geochemical

13 characterization, The Cryosphere, 13, 1147-1165, 10.5194/tc-13-1147-2019, 2019.

14 Doelling, D. R., Loeb, N. G., Keyes, D. F., Nordeen, M. L., Morstad, D., Nguyen, C.,

15 Wielicki, B. A., Young, D. F., and Sun, M.: Geostationary Enhanced Temporal

16 Interpolation for CERES Flux Products, Journal of Atmospheric and Oceanic

17 Technology, 30, 1072-1090, 10.1175/jtech-d-12-00136.1, 2013.

18 Doherty, S. J., Warren, S. G., Grenfell, T. C., Clarke, A. D., and Brandt, R. E.: Light-

19 absorbing impurities in Arctic snow, Atmospheric Chemistry and Physics, 10, 11647-

20 11680, 10.5194/acp-10-11647-2010, 2010.

Doherty, S. J., Dang, C., Hegg, D. A., Zhang, R., and Warren, S. G.: Black carbon and other light-absorbing particles in snow of central North America, Journal of Geophysical Research: Atmospheres, 119, 12,807-812,831, 10.1002/2014jd022350, 2014.

Dozier, J., and Marks, D.: Snow Mapping and Classification from Landsat Thematic Mapper Data, Annals of Glaciology, 9, 97-103, https://doi.org/10.3189/S026030550000046X, 1987.

Drusch, M., Vasiljevic, D., and Viterbo, P.: ECMWF's Global Snow Analysis: Assessment and Revision Based on Satellite Observations, Journal of Applied Meteorology, 43, 1282-1294, 10.1175/1520-0450(2004)043<1282:egsaaa>2.0.co;2, 2004.

Eyring, V., Bony, S., Meehl, G. A., Senior, C. A., Stevens, B., Stouffer, R. J., and Taylor, K. E.: Overview of the Coupled Model Intercomparison Project Phase 6 (CMIP6) experimental design and organization, Geosci Model Dev, 9, 1937-1958, 10.5194/gmd-9-1937-2016, 2016.

Flanner, M. G., Zender, C. S., Randerson, J. T., and Rasch, P. J.: Present-day climate forcing and response from black carbon in snow, Journal of Geophysical Research, 112, 10.1029/2006jd008003, 2007.

Flanner, M. G., Zender, C. S., Hess, P. G., Mahowald, N. M., Painter, T. H., Ramanathan, V., and Rasch, P. J.: Springtime warming and reduced snow cover from carbonaceous

particles, Atmospheric Chemistry and Physics, 9, 2481-2497, 10.5194/acp-9-2481-2009, 2009.

Flanner, M. G., Shell, K. M., Barlage, M., Perovich, D. K., and Tschudi, M. A.: Radiative forcing and albedo feedback from the Northern Hemisphere cryosphere between 1979 and 2008, Nature Geoscience, 4, 151-155, 10.1038/ngeo1062, 2011.

Flanner, M. G., Gardner, A. S., Eckhardt, S., Stohl, A., and Perket, J.: Aerosol radiative forcing from the 2010 Eyjafjallajökull volcanic eruptions, Journal of Geophysical Research: Atmospheres, 119, 9481-9491, 10.1002/2014jd021977, 2014.

Fu, Y., Zhu, J., Yang, Y., Yuan, R., Liu, G., Xian, T., and Liu, P.: Grid-cell aerosol direct shortwave radiative forcing calculated using the SBDART model with MODIS and AERONET observations: An application in winter and summer in eastern China, Advances in Atmospheric Sciences, 34, 952-964, 10.1007/s00376-017-6226-z, 2017.

Ganey, G. Q., Loso, M. G., Burgess, A. B., and Dial, R. J.: The role of microbes in snowmelt and radiative forcing on an Alaskan icefield, Nature Geoscience, 10, 754-759, 10.1038/ngeo3027, 2017.

Grell, G. A., Peckham, S. E., Schmitz, R., McKeen, S. A., Frost, G., Skamarock, W. C., and Eder, B.: Fully coupled "online" chemistry within the WRF model, Atmospheric Environment, 39, 6957-6975, 10.1016/j.atmosenv.2005.04.027, 2005.

Grenfell, T. C., Doherty, S. J., Clarke, A. D., and Warren, S. G.: Light absorption from particulate impurities in snow and ice determined by spectrophotometric analysis of

1 filters, Appl Opt, 50, 2037-2048, 10.1364/AO.50.002037, 2011.

2 Hadley, O. L., and Kirchstetter, T. W.: Black-carbon reduction of snow albedo, Nature

3 Climate Change, 2, 437-440, 10.1038/nclimate1433, 2012.

4 Hall, A., and Qu, X.: Using the current seasonal cycle to constrain snow albedo

5 feedback in future climate change, Geophysical Research Letters, 33,

6 10.1029/2005gl025127, 2006.

7 Hall, D. K., Riggs, G. A., and Salomonson, V. V.: Development of methods for mapping

8 global snow cover using moderate resolution imaging spectroradiometer data, Remote

9 Sensing of Environment, 54, 127-140, 10.1016/0034-4257(95)00137-p, 1995.

10 Hansen, J., and Nazarenko, L.: Soot climate forcing via snow and ice albedos, P Natl

11 Acad Sci USA, 101, 423-428, 2004.

12 Hegg, D. A., Warren, S. G., Grenfell, T. C., Doherty, S. J., Larson, T. V., and Clarke, A.

13 D.: Source attribution of black carbon in Arctic snow, Environ Sci Technol, 43, 4016-

14 4021, 10.1021/es803623f, 2009.

15 Huang, J. P. and Yi, Y. H.: Inversion of a nonlinear dynamic-model from the observation,

16 Sci. China Chem., 34, 1246–1246, 1991.

17 Huang, J., Fu, Q., Zhang, W., Wang, X., Zhang, R., Ye, H., and Warren, S. G.: Dust and

18 Black Carbon in Seasonal Snow Across Northern China, Bulletin of the American

19 Meteorological Society, 92, 175-181, 10.1175/2010bams3064.1, 2011.

1   Kaspari, S., Painter, T. H., Gysel, M., Skiles, S. M., and Schwikowski, M.: Seasonal

2   and elevational variations of black carbon and dust in snow and ice in the Solu-Khumbu,

3   Nepal and estimated radiative forcings, Atmospheric Chemistry and Physics, 14, 8089-

4   8103, 10.5194/acp-14-8089-2014, 2014.

5   Kaspari, S., McKenzie Skiles, S., Delaney, I., Dixon, D., and Painter, T. H.: Accelerated

6   glacier melt on Snow Dome, Mount Olympus, Washington, USA, due to deposition of

7   black carbon and mineral dust from wildfire, Journal of Geophysical Research:

8   Atmospheres, 120, 2793-2807, 10.1002/2014jd022676, 2015.

9   Lee, L. A., Reddington, C. L., and Carslaw, K. S.: On the relationship between aerosol

10   model uncertainty and radiative forcing uncertainty, Proc Natl Acad Sci U S A, 113,

11   5820-5827, 10.1073/pnas.1507050113, 2016.

12   Lewis, P., and Barnsley, M.: Influence of the sky radiance distribution on various

13   formulations of the earth surface albedo, 6th International Symposium on Physical

14   Measurements and Signatures in Remote Sensing, ISPRS, 1994, 707-715,

15   Liou, K. N., Takano, Y., He, C., Yang, P., Leung, L. R., Gu, Y., and Lee, W. L.:

16   Stochastic parameterization for light absorption by internally mixed BC/dust in snow

17   grains for application to climate models, Journal of Geophysical Research:

18   Atmospheres, 119, 7616-7632, 10.1002/2014jd021665, 2014.

19   Loeb, N. G., Doelling, D. R., Wang, H., Su, W., Nguyen, C., Corbett, J. G., Liang, L.,

20   Mitrescu, C., Rose, F. G., and Kato, S.: Clouds and the Earth's Radiant Energy System

(CERES) Energy Balanced and Filled (EBAF) Top-of-Atmosphere (TOA) Edition-4.0 Data Product, Journal of Climate, 31, 895-918, 10.1175/jcli-d-17-0208.1, 2018.

Meinander, O., Kazadzis, S., Arola, A., Riihelä, A., Räisänen, P., Kivi, R., Kontu, A., Kouznetsov, R., Sofiev, M., Svensson, J., Suokanerva, H., Aaltonen, V., Manninen, T., Roujean, J. L., and Hautecoeur, O.: Spectral albedo of seasonal snow during intensive melt period at Sodankylä, beyond the Arctic Circle, Atmospheric Chemistry and Physics, 13, 3793-3810, 10.5194/acp-13-3793-2013, 2013.

Miller, S. D., Wang, F., Burgess, A. B., Skiles, S. M., Rogers, M., and Painter, T. H.: Satellite-Based Estimation of Temporally Resolved Dust Radiative Forcing in Snow Cover, Journal of Hydrometeorology, 17, 1999-2011, 2016.

Nagorski, S. A., Kaspari, S. D., Hood, E., Fellman, J. B., and Skiles, S. M.: Radiative Forcing by Dust and Black Carbon on the Juneau Icefield, Alaska, Journal of Geophysical Research: Atmospheres, 124, 3943-3959, 10.1029/2018jd029411, 2019.

Negi, H. S., and Kokhanovsky, A.: Retrieval of snow grain size and albedo of western Himalayan snow cover using satellite data, The Cryosphere, 5, 831-847, 10.5194/tc-5-831-2011, 2011.

Nolin, A. W., and Dozier, J.: Estimating snow grain size using AVIRIS data, Remote Sensing of Environment, 44, 231-238, 10.1016/0034-4257(93)90018-s, 1993.

Nolin, A. W., and Dozier, J.: A Hyperspectral Method for Remotely Sensing the Grain Size of Snow, Remote Sensing of Environment, 74, 207-216, 10.1016/s0034-

4257(00)00111-5, 2000.

Nowottnick, E., Colarco, P., Ferrare, R., Chen, G., Ismail, S., Anderson, B., and Browell, E.: Online simulations of mineral dust aerosol distributions: Comparisons to NAMMA observations and sensitivity to dust emission parameterization, Journal of Geophysical Research, 115, 10.1029/2009jd012692, 2010.

Nowottnick, E., Colarco, P., da Silva, A., Hlavka, D., and McGill, M.: The fate of saharan dust across the atlantic and implications for a central american dust barrier, Atmospheric Chemistry and Physics, 11, 8415-8431, 10.5194/acp-11-8415-2011, 2011.

Oaida, C. M., Xue, Y., Flanner, M. G., Skiles, S. M., De Sales, F., and Painter, T. H.: Improving snow albedo processes in WRF/SSiB regional climate model to assess impact of dust and black carbon in snow on surface energy balance and hydrology over western U.S, Journal of Geophysical Research: Atmospheres, 120, 3228-3248, 10.1002/2014jd022444, 2015.

Painter, T. H., Roberts, D. A., Green, R. O., and Dozier, J.: The Effect of Grain Size on Spectral Mixture Analysis of Snow-Covered Area from AVIRIS Data, Remote Sensing of Environment, 65, 320-332, 10.1016/s0034-4257(98)00041-8, 1998.

Painter, T. H., Barrett, A. P., Landry, C. C., Neff, J. C., Cassidy, M. P., Lawrence, C. R., McBride, K. E., and Farmer, G. L.: Impact of disturbed desert soils on duration of mountain snow cover, Geophysical Research Letters, 34, 10.1029/2007gl030284, 2007.

Painter, T. H., Rittger, K., McKenzie, C., Slaughter, P., Davis, R. E., and Dozier, J.:

Retrieval of subpixel snow covered area, grain size, and albedo from MODIS, Remote

Sensing of Environment, 113, 868-879, 10.1016/j.rse.2009.01.001, 2009.

Painter, T. H., Deems, J. S., Belnap, J., Hamlet, A. F., Landry, C. C., and Udall, B.:

Response of Colorado River runoff to dust radiative forcing in snow, Proc Natl Acad

Sci U S A, 107, 17125-17130, 10.1073/pnas.0913139107, 2010.

Painter, T. H., Bryant, A. C., and Skiles, S. M.: Radiative forcing by light absorbing

impurities in snow from MODIS surface reflectance data, Geophysical Research

Letters, 39, n/a-n/a, 10.1029/2012gl052457, 2012a.

Painter, T. H., Skiles, S. M., Deems, J. S., Bryant, A. C., and Landry, C. C.: Dust

radiative forcing in snow of the Upper Colorado River Basin: 1. A 6 year record of

energy balance, radiances, and dust concentrations, Water Resources Research, 48,

10.1029/2012wr011985, 2012b.

Painter, T. H., Seidel, F. C., Bryant, A. C., McKenzie Skiles, S., and Rittger, K.: Imaging

spectroscopy of albedo and radiative forcing by light-absorbing impurities in mountain

snow, Journal of Geophysical Research: Atmospheres, 118, 9511-9523,

10.1002/jgrd.50520, 2013.

Pu, W., Wang, X., Wei, H., Zhou, Y., Shi, J., Hu, Z., Jin, H., and Chen, Q.: Properties

of black carbon and other insoluble light-absorbing particles in seasonal snow of

northwestern China, The Cryosphere, 11, 1213-1233, 10.5194/tc-11-1213-2017, 2017.

Pu, W., Cui, J., Shi, T., Zhang, X., He, C., and Wang, X.: The remote sensing of radiative

forcing by light-absorbing particles (LAPs) in seasonal snow over northeastern China, Atmospheric Chemistry and Physics, 19, 9949-9968, 10.5194/acp-19-9949-2019, 2019.

Qi, L., Li, Q., Henze, D. K., Tseng, H.-L., and He, C.: Sources of springtime surface black carbon in the Arctic: an adjoint analysis for April 2008, Atmospheric Chemistry and Physics, 17, 9697-9716, 10.5194/acp-17-9697-2017, 2017.

Qian, Y., Gustafson, W. I., Leung, L. R., and Ghan, S. J.: Effects of soot-induced snow albedo change on snowpack and hydrological cycle in western United States based on Weather Research and Forecasting chemistry and regional climate simulations, Journal of Geophysical Research, 114, 10.1029/2008jd011039, 2009.

Qian, Y., Flanner, M. G., Leung, L. R., and Wang, W.: Sensitivity studies on the impacts of Tibetan Plateau snowpack pollution on the Asian hydrological cycle and monsoon climate, Atmospheric Chemistry and Physics, 11, 1929-1948, 10.5194/acp-11-1929-2011, 2011.

Qian, Y., Wang, H., Zhang, R., Flanner, M. G., and Rasch, P. J.: A sensitivity study on modeling black carbon in snow and its radiative forcing over the Arctic and Northern China, Environmental Research Letters, 9, 064001, 10.1088/1748-9326/9/6/064001, 2014.

Qian, Y., Yasunari, T. J., Doherty, S. J., Flanner, M. G., Lau, W. K. M., Ming, J., Wang, H., Wang, M., Warren, S. G., and Zhang, R.: Light-absorbing particles in snow and ice: Measurement and modeling of climatic and hydrological impact, Advances in

Atmospheric Sciences, 32, 64-91, 10.1007/s00376-014-0010-0, 2015.

Ramanathan, V., and Carmichael, G.: Global and regional climate changes due to black carbon, Nature Geoscience, 1, 221-227, 10.1038/ngeo156, 2008.

Randles, C. A., da Silva, A. M., Buchard, V., Colarco, P. R., Darmenov, A., Govindaraju, R., Smirnov, A., Holben, B., Ferrare, R., Hair, J., Shinozuka, Y., and Flynn, C. J.: The MERRA-2 Aerosol Reanalysis, 1980 Onward. Part I: System Description and Data Assimilation Evaluation, Journal of Climate, 30, 6823-6850, 10.1175/jcli-d-16-0609.1, 2017.

Ricchiazzi, P., Yang, S., Gautier, C., and Sowle, D.: SBDART: A Research and Teaching Software Tool for Plane-Parallel Radiative Transfer in the Earth's Atmosphere, Bulletin of the American Meteorological Society, 79, 2101-2114, 10.1175/1520-0477(1998)079<2101:sarats>2.0.co;2, 1998.

Riggs G A, Hall D K, Román M O. MODIS snow products collection 6 user guide. National Snow and Ice Data Center: Boulder, CO, USA, 2016.

Rittger, K., Painter, T. H., and Dozier, J.: Assessment of methods for mapping snow cover from MODIS, Advances in Water Resources, 51, 367-380,10.1016/j.advwatres.2012.03.002, 2013.

Sarangi, C., Qian, Y., Rittger, K., Bormann, K. J., Liu, Y., Wang, H., Wan, H., Lin, G., and Painter, T. H.: Impact of light-absorbing particles on snow albedo darkening and associated radiative forcing over high-mountain Asia: high-resolution WRF-Chem

modeling and new satellite observations, Atmospheric Chemistry and Physics, 19, 7105-7128, 10.5194/acp-19-7105-2019, 2019.

Seidel, F. C., Rittger, K., Skiles, S. M., Molotch, N. P., and Painter, T. H.: Case study of spatial and temporal variability of snow cover, grain size, albedo and radiative forcing in the Sierra Nevada and Rocky Mountain snowpack derived from imaging spectroscopy, The Cryosphere, 10, 1229-1244, 10.5194/tc-10-1229-2016, 2016.

Siegmund, A. and Menz, G.: Fernes nah gebracht–Satelliten-undLuftbildeinsatz zur Analyse von Umweltveränderungen im Geographieunterricht, Geographie und Schule, 154, 2–10, 2005.

Shi, T., Pu, W., Zhou, Y., Cui, J., Zhang, D., and Wang, X.: Albedo of Black Carbon-Contaminated Snow Across Northwestern China and the Validation With Model Simulation, Journal of Geophysical Research: Atmospheres, 125, e2019JD032065, 10.1029/2019JD032065, 2020.

Skamarock, W. C., Klemp, J. B., Dudhia, J., Gill, D. O., Barker,D. M., Duda, M. G., Huang, X., Wang, W., and Powers, J. G.:A description of the advanced research WRF version 3, NCARTech. Note, NCAR/TN-475+STR, 8 pp., Natl. Cent. for Atmos.Res., Boulder, Colo., 2008 (available at: http://www.mmm.ucar.edu/wrf/users/docs/arw_v3.pdf)

Skiles, S. M., and Painter, T.: Daily evolution in dust and black carbon content, snow grain size, and snow albedo during snowmelt, Rocky Mountains, Colorado, J Glaciol,

63, 118-132, 10.1017/jog.2016.125, 2016.

Skiles, S. M., Flanner, M., Cook, J. M., Dumont, M., and Painter, T. H.: Radiative forcing by light-absorbing particles in snow, Nature Climate Change, 8, 964-971, 10.1038/s41558-018-0296-5, 2018.

Solomos, S., Ansmann, A., Mamouri, R.-E., Binietoglou, I., Patlakas, P., Marinou, E., and Amiridis, V.: Remote sensing and modelling analysis of the extreme dust storm hitting the Middle East and eastern Mediterranean in September 2015, Atmospheric Chemistry and Physics, 17, 4063-4079, 10.5194/acp-17-4063-2017, 2017.

Stamnes, K., Tsay, S. C., Wiscombe, W., and Jayaweera, K.: Numerically stable algorithm for discrete-ordinate-method radiative transfer in multiple scattering and emitting layered media, Appl Opt, 27, 2502-2509, 10.1364/AO.27.002502, 1988.

Sterle, K. M., McConnell, J. R., Dozier, J., Edwards, R., and Flanner, M. G.: Retention and radiative forcing of black carbon in eastern Sierra Nevada snow, The Cryosphere, 7, 365-374, 10.5194/tc-7-365-2013, 2013.

Sturm, M., Holmgren, J., and Liston, G. E.: A Seasonal Snow Cover Classification System for Local to Global Applications, Journal of Climate, 8, 1261-1283, 10.1175/1520-0442(1995)008<1261:assccs>2.0.co;2, 1995.

Su, W., Corbett, J., Eitzen, Z., and Liang, L.: Next-generation angular distribution models for top-of-atmosphere radiative flux calculation from CERES instruments: validation, Atmospheric Measurement Techniques, 8, 3297-3313, 10.5194/amt-8-3297-

2015, 2015.

TanrÉ, D., Deroo, C., Duhaut, P., Herman, M., Morcrette, J. J., Perbos, J., and Deschamps, P. Y.: Technical note Description of a computer code to simulate the satellite signal in the solar spectrum: the 5S code, International Journal of Remote Sensing, 11, 659-668, 10.1080/01431169008955048, 1990.

Tedesco, M., and Kokhanovsky, A. A.: The semi-analytical snow retrieval algorithm and its application to MODIS data, Remote Sensing of Environment, 111, 228-241, 10.1016/j.rse.2007.02.036, 2007.

Teillet, P. M., Guindon, B., and Goodenough, D. G.: On the Slope-Aspect Correction of Multispectral Scanner Data, Canadian Journal of Remote Sensing, 8, 84-106, 10.1080/07038992.1982.10855028, 1982.

Toon, O. B., McKay, C. P., Ackerman, T. P., and Santhanam, K.: Rapid calculation of radiative heating rates and photodissociation rates in inhomogeneous multiple scattering atmospheres, Journal of Geophysical Research, 94, 16287, 10.1029/JD094iD13p16287, 1989.

Wang, R., Tao, S., Shen, H., Wang, X., Li, B., Shen, G., Wang, B., Li, W., Liu, X., Huang, Y., Zhang, Y., Lu, Y., and Ouyang, H.: Global emission of black carbon from motor vehicles from 1960 to 2006, Environ Sci Technol, 46, 1278-1284, 10.1021/es2032218, 2012.

Wang, R., Tao, S., Ciais, P., Shen, H. Z., Huang, Y., Chen, H., Shen, G. F., Wang, B.,

Li, W., Zhang, Y. Y., Lu, Y., Zhu, D., Chen, Y. C., Liu, X. P., Wang, W. T., Wang, X. L., Liu, W. X., Li, B. G., and Piao, S. L.: High-resolution mapping of combustion processes and implications for CO2 emissions, Atmospheric Chemistry and Physics, 13, 5189-5203, 10.5194/acp-13-5189-2013, 2013a.

Wang, R., Tao, S., Shen, H., Huang, Y., Chen, H., Balkanski, Y., Boucher, O., Ciais, P., Shen, G., Li, W., Zhang, Y., Chen, Y., Lin, N., Su, S., Li, B., Liu, J., and Liu, W.: Trend in global black carbon emissions from 1960 to 2007, Environ Sci Technol, 48, 6780-6787, 10.1021/es5021422, 2014a.

Wang, X., Doherty, S. J., and Huang, J.: Black carbon and other light-absorbing impurities in snow across Northern China, Journal of Geophysical Research: Atmospheres, 118, 1471-1492, 10.1029/2012jd018291, 2013b.

Wang, X., Pu, W., Ren, Y., Zhang, X., Zhang, X., Shi, J., Jin, H., Dai, M., and Chen, Q.: Observations and model simulations of snow albedo reduction in seasonal snow due to insoluble light-absorbing particles during 2014 Chinese survey, Atmospheric Chemistry and Physics, 17, 2279-2296, 10.5194/acp-17-2279-2017, 2017.

Wang, X., Wei, H. L., Liu, J., Xu, B. Q., Wang, M., Ji, M. X., and Jin, H. C.: Quantifying the light absorption and source attribution of insoluble light-absorbing particles on Tibetan Plateau glaciers between 2013 and 2015, Cryosphere, 13, 309-324, 10.5194/tc-13-309-2019, 2019.

Wang, X., Xu, B., and Ming, J.: An overview of the studies on black carbon and mineral

dust deposition in snow and ice cores in East Asia, Journal of Meteorological Research, 28, 354-370, 10.1007/s13351-014-4005-7, 2014b.

Wang, X., Zhang, X., and Di, W.: Development of an improved two-sphere integration technique for quantifying black carbon concentrations in the atmosphere and seasonal snow, Atmospheric Measurement Techniques, 13, 39-52, 10.5194/amt-13-39-2020, 2020.

Warneke, C., Froyd, K. D., Brioude, J., Bahreini, R., Brock, C. A., Cozic, J., de Gouw, J. A., Fahey, D. W., Ferrare, R., Holloway, J. S., Middlebrook, A. M., Miller, L., Montzka, S., Schwarz, J. P., Sodemann, H., Spackman, J. R., and Stohl, A.: An important contribution to springtime Arctic aerosol from biomass burning in Russia, Geophysical Research Letters, 37, n/a-n/a, 10.1029/2009gl041816, 2010.

Warren, S. G.: Optical properties of snow, Reviews of Geophysics, 20, 67, 10.1029/RG020i001p00067, 1982.

Warren, S. G.: Impurities in Snow: Effects on Albedo and Snowmelt (Review), Annals of Glaciology, 5, 177-179, 10.3189/1984AoG5-1-177-179, 1984.

Warren, S. G., and Brandt, R. E.: Optical constants of ice from the ultraviolet to the microwave: A revised compilation, Journal of Geophysical Research, 113, 10.1029/2007jd009744, 2008.

Warren, S. G.: Can black carbon in snow be detected by remote sensing?, Journal of Geophysical Research: Atmospheres, 118, 779-786, 10.1029/2012jd018476, 2013.

Wiscombe, W. J., and Warren, S. G.: A Model for the Spectral Albedo of Snow. I: Pure Snow, Journal of the Atmospheric Sciences, 37, 2712-2733, 10.1175/1520-0469(1980)037<2712:amftsa>2.0.co;2, 1980.

Ye, H., Zhang, R., Shi, J., Huang, J., Warren, S. G., and Fu, Q.: Black carbon in seasonal snow across northern Xinjiang in northwestern China, Environmental Research Letters, 7, 044002, 10.1088/1748-9326/7/4/044002, 2012.

Zhao, C., Hu, Z., Qian, Y., Ruby Leung, L., Huang, J., Huang, M., Jin, J., Flanner, M. G., Zhang, R., Wang, H., Yan, H., Lu, Z., and Streets, D. G.: Simulating black carbon and dust and their radiative forcing in seasonal snow: a case study over North China with field campaign measurements, Atmospheric Chemistry and Physics, 14, 11475-11491, 10.5194/acp-14-11475-2014, 2014.

Zhong, E., Li, Q., Sun, S., Chen, S., and Chen, W.: Analysis of euphotic depth in snow with SNICAR transfer scheme, Atmospheric Science Letters, 18, 484-490, 10.1002/asl.792, 2017.

Zhou, Y., Wen, H., Liu, J., Pu, W., Chen, Q. C., and Wang, X.: The optical characteristics and sources of chromophoric dissolved organic matter (CDOM) in seasonal snow of northwestern China, Cryosphere, 13, 157-175, 10.5194/tc-13-157-2019, 2019.

Zhu, C., Kobayashi, H., Kanaya, Y., and Saito, M.: Size-dependent validation of MODIS MCD64A1 burned area over six vegetation types in boreal Eurasia: Large underestimation in croplands, Sci Rep, 7, 4181, 10.1038/s41598-017-03739-0, 2017.
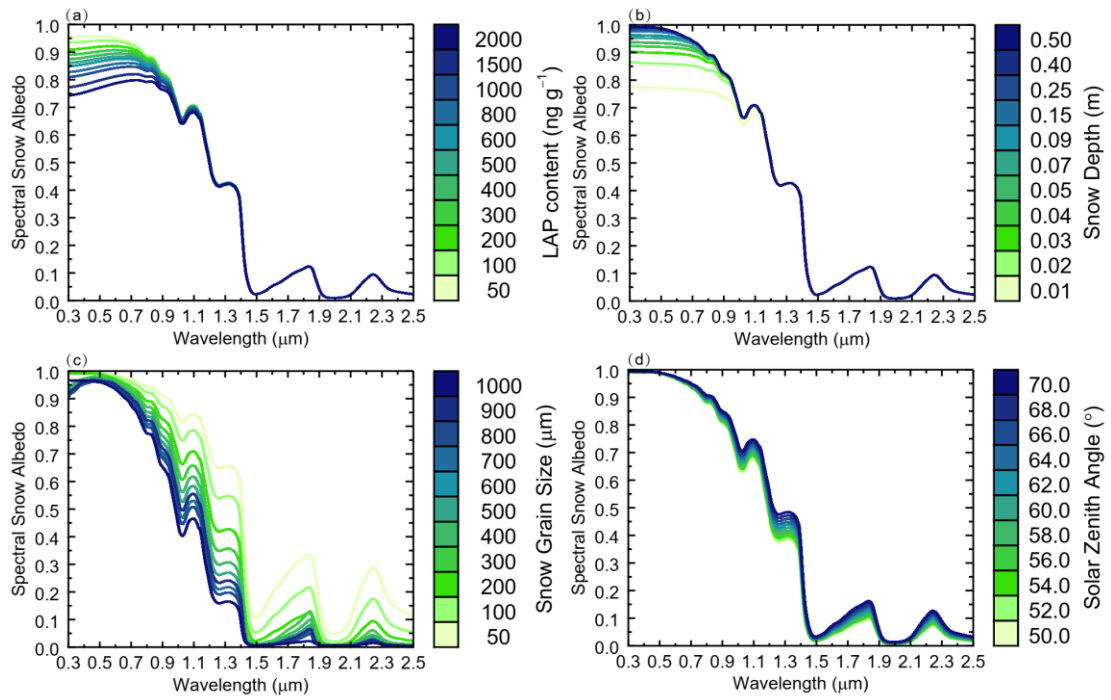
2 Figure 1. Variations in spectral snow albedo due to (a) LAP content (ng g^{-1}), (b) snow depth (m), (c)

3 snow grain size (µm), and (d) solar zenith angle (deg.).
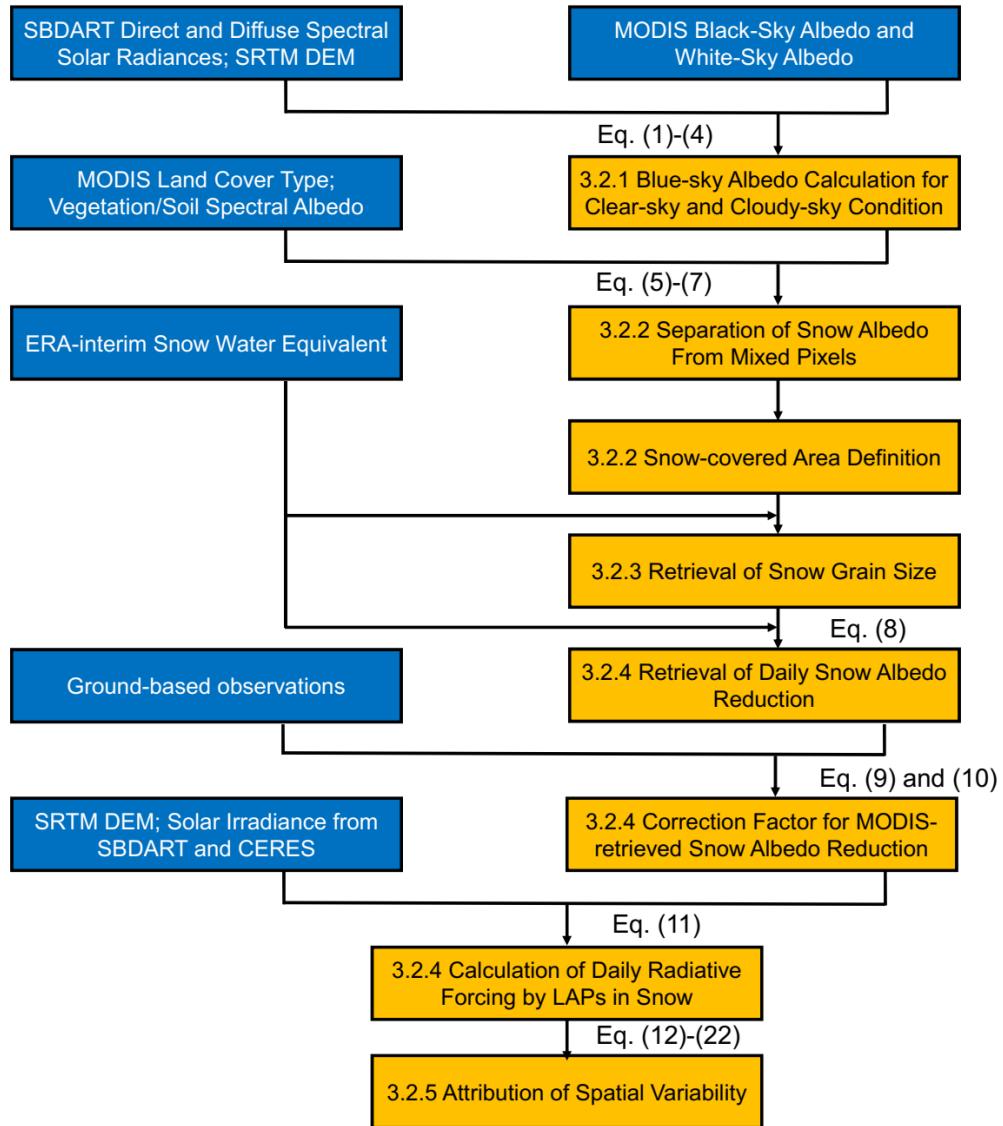
2   Figure 2. Workflow depicting the calculation and validation of radiative forcing of LAPs in snow:

3   the blue boxes denote the external input data, while the orange boxes are used for calculations in

4   this study.
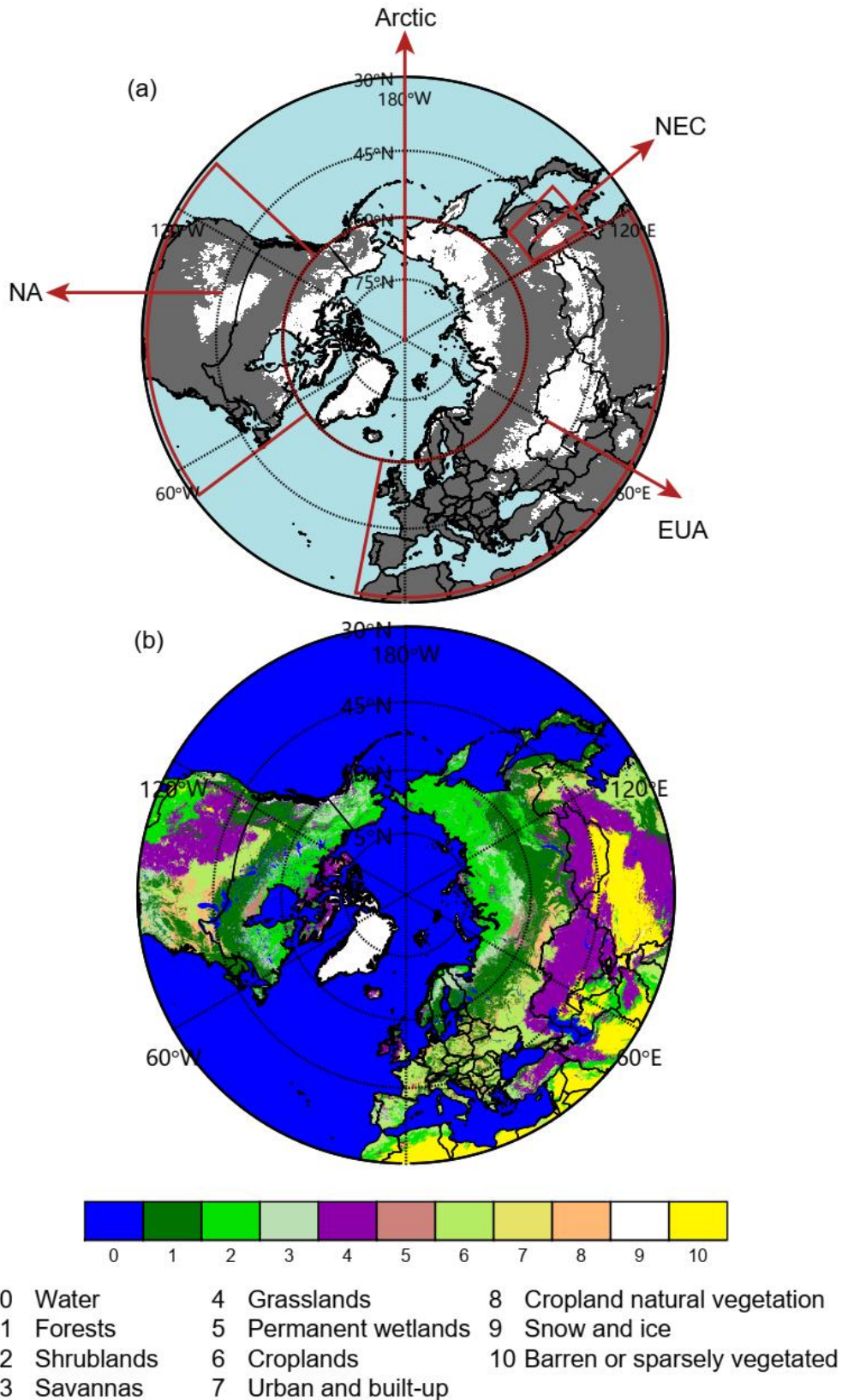
Figure 3. Spatial distributions of (a) identified snow-covered areas (ISCA) and (b) the different land-

cover types, based on MODIS data, for the Northern Hemisphere. ISCA (white) can be separated

1   into northeastern China (NEC), Eurasia (EUA), North America (NA), and the Arctic.
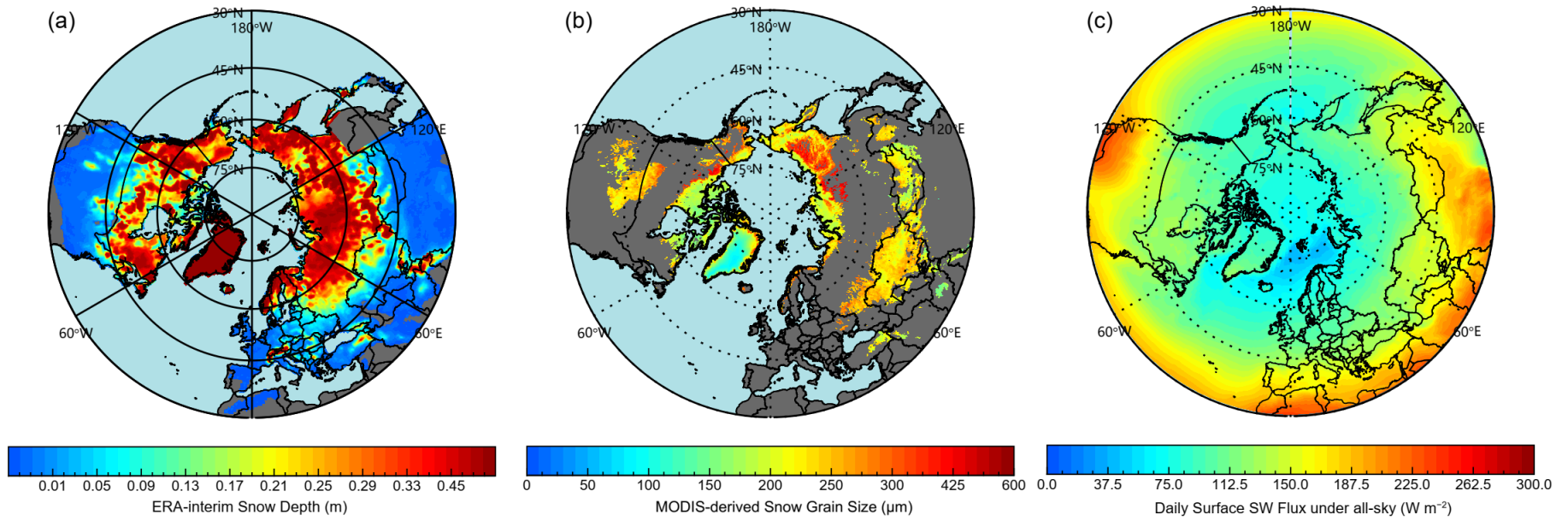
Figure 4. Spatial distributions of 2003-2018 averaged (a) snow depth from ERA-interim, (d) snow grain size retrieved by MODIS, and (c) total downward shortwave flux at the surface during December-May from CERES.
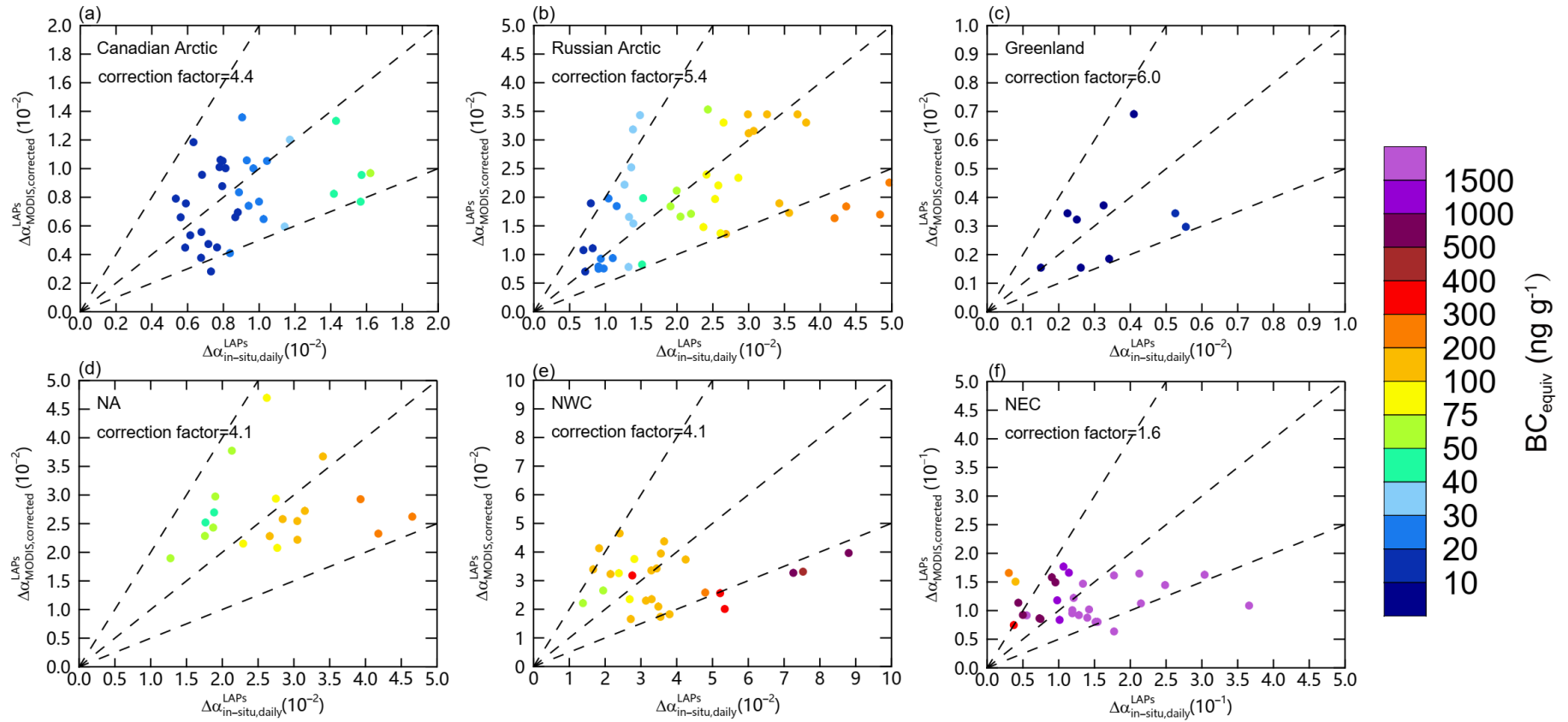
3   Figure 5. Scatterplots of $\Delta\alpha_{MODIS,corrected}^{LAPs}$ versus $\Delta\alpha_{in-situ,daily}^{LAPs}$. Panels (a)–(f) represent the snow samples collected in Canadian Arctic, Russian Arctic, Greenland,

4   North America, Northwestern China, and Northeastern China, respectively.
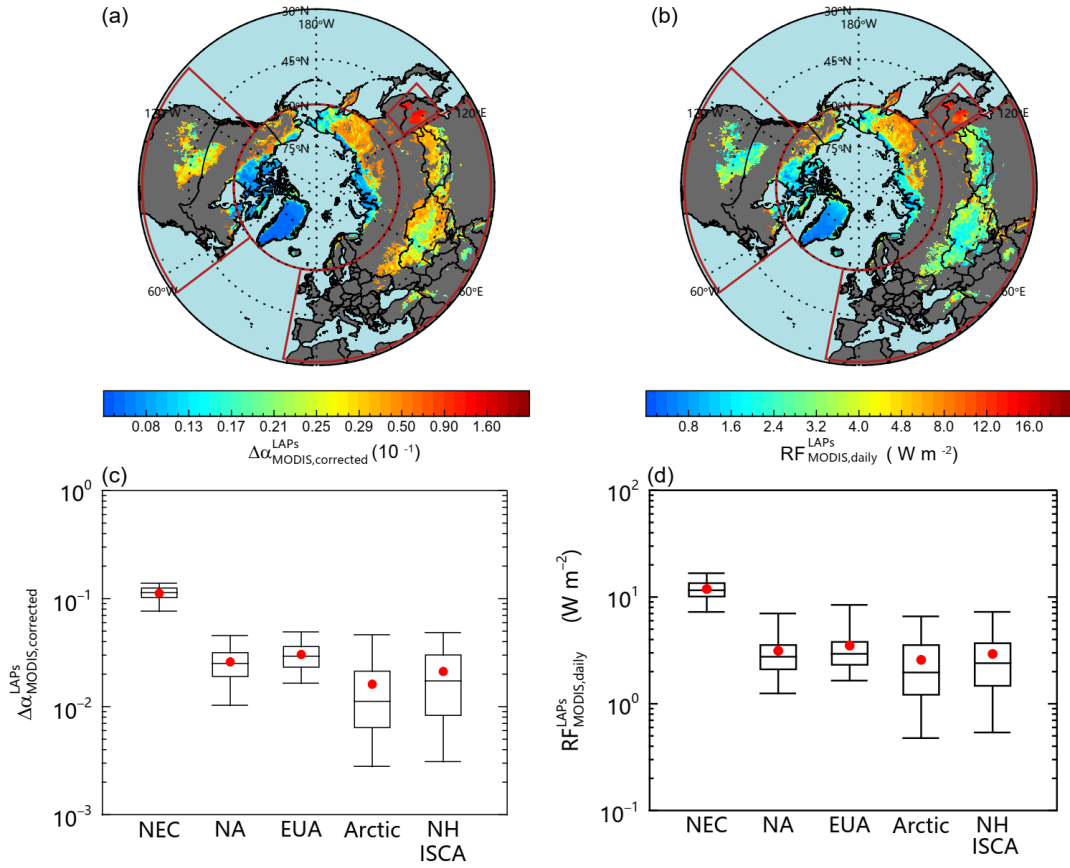
Figure 6. Spatial distributions of averaged (a) $\Delta\alpha_{MODIS,corrected}^{LAPs}$, (b) $RF_{MODIS,daily}^{LAPs}$ and statistics for regionally averaged (c) $\Delta\alpha_{MODIS,corrected}^{LAPs}$ and (d) $RF_{MODIS,daily}^{LAPs}$ for the Northern Hemisphere ISCA in December-May during the period 2003–2018. The boxes denote the 25th and 75th quantiles, and the horizontal lines represent the 50th quantiles (medians), the averages are shown as red dots; the whiskers denote the 5th and 95th quantiles.
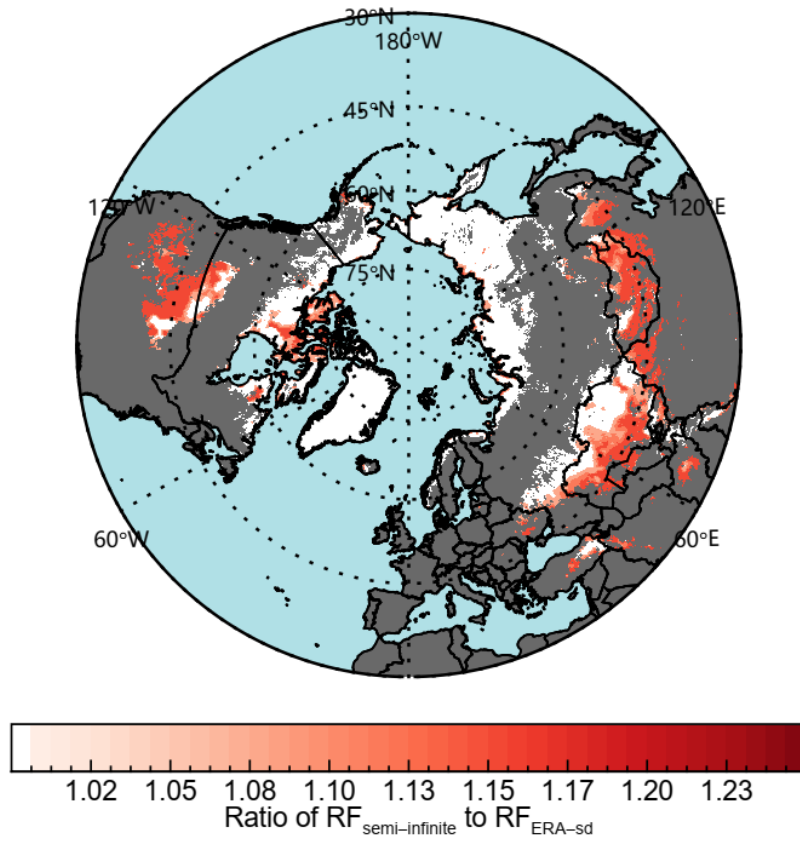
2 Figure 7. The spatial distribution of the ratio of retrieved radiative forcing using semi-infinite snow

3 to radiative forcing using ERA-Interim snow depth.
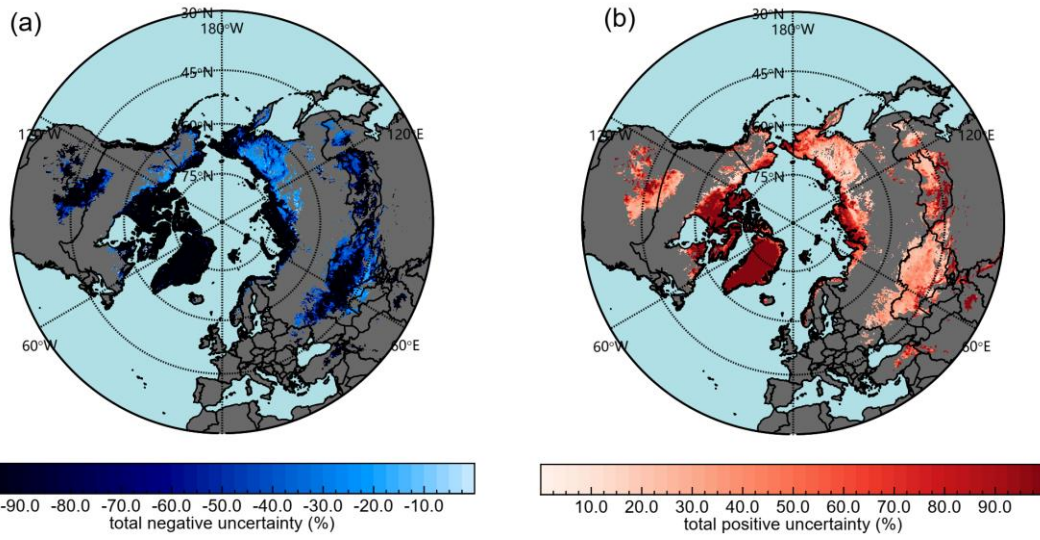
2   Figure 8. The overall uncertainty of radiative forcing retrieval due to atmospheric correction,

3   MODIS-derived snow grain size retrieval and snow cover fraction calculation.
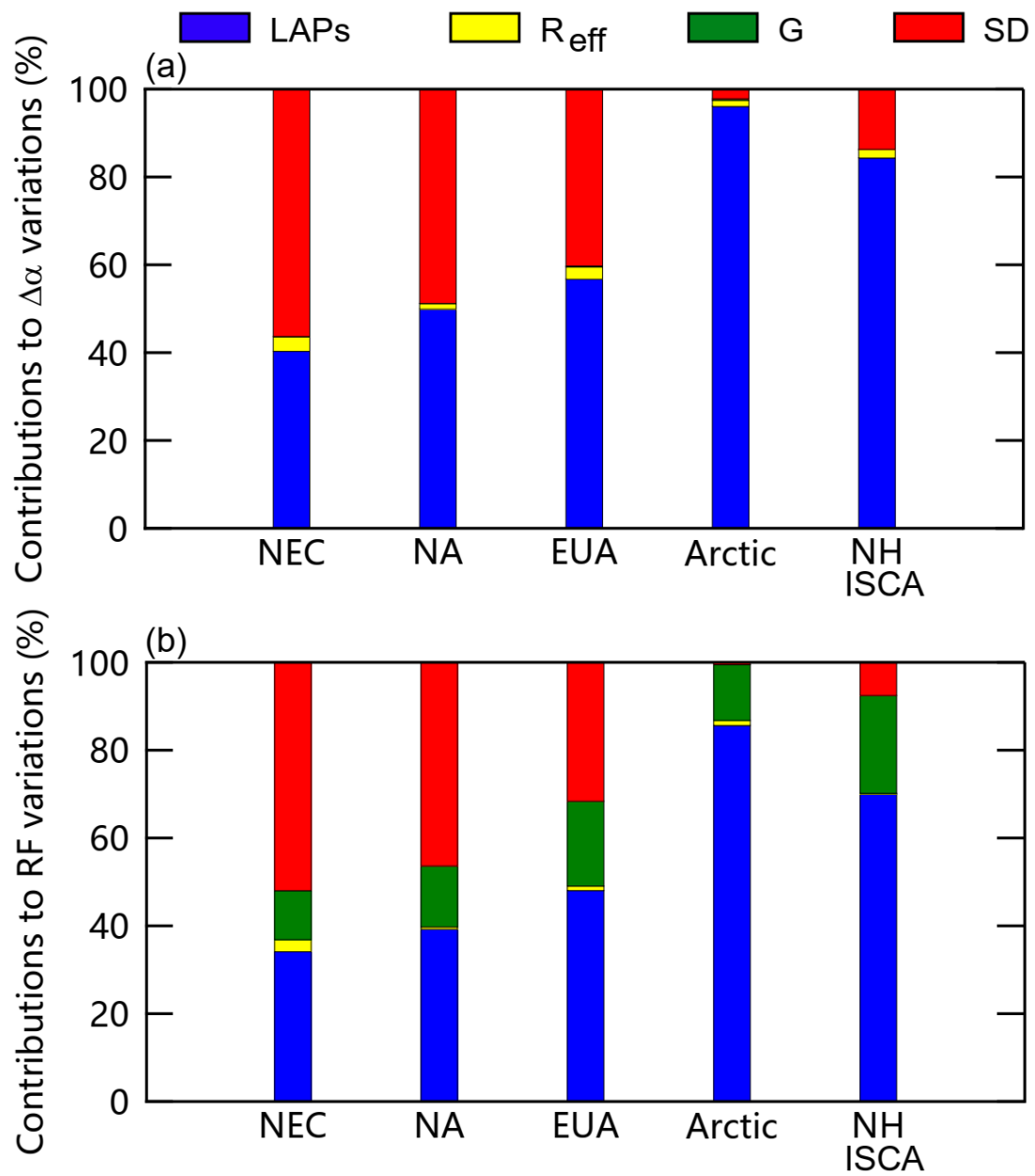
Figure 9. Fractional contributions of LAPs, snow grain size (R_{eff}), geographic factor (G), and snow depth (SD) to the spatial variations of (a) snow albedo reduction and (b) daily radiative forcing.
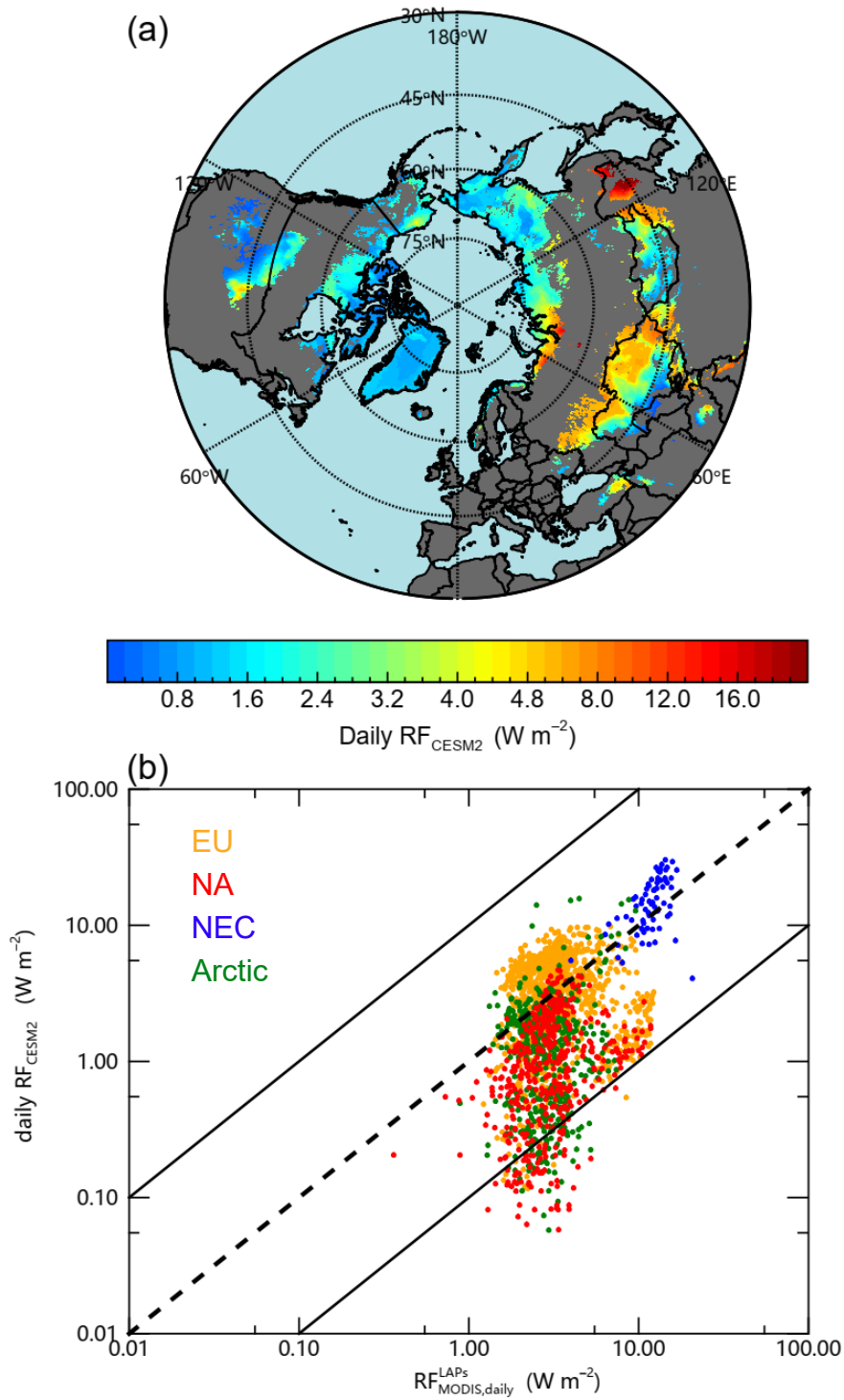
Figure 10. (a) Spatial distributions of average-daily radiative forcing (RF_{CESM2}), based on the
CESM2 soot content of snow in December-May for the period 2003–2014. (b) Scatterplot of
$RF_{MODIS,daily}^{LAPs}$ versus RF_{CESM2}.

Table 1. Statistics for regionally averaged (5th and 95th quantiles) albedo reduction ($\Delta\alpha_{MODIS,corrected}^{LAPs}$) and daily radiative forcing ($RF_{MODIS,daily}^{LAPs}$, W m^{-2})

	Northeastern China	EUA	NA	Canadian Arctic	Greenland	Russian Arctic	ISCA over Northern Hemisphere
Albedo reduction ($\Delta\alpha_{MODIS,corrected}^{LAPs}$)	0.11 (0.077~0.14)	0.031 (0.017~0.049)	0.027 (0.014~0.046)	0.025 (0.012~0.055)	0.016 (0.011~0.023)	0.028 (0.012~0.048)	0.021 (0.0031~0.049)
Daily radiative forcing ($RF_{MODIS,daily}^{LAPs}$, W m^{-2})	12 (7.2~17)	3.5 (1.6~8.4)	3.1 (1.3~7.0)	2.6 (0.59~6.1)	1.3 (0.40~3.3)	3.3 (1.0~7.3)	2.9 (0.54~7.3)

2
3   Table.2 Comparisons of radiative forcing due to LAPs in snow (this study) with observed and model-simulated values from previous studies

Study	Region	Time period	Method	Radiative forcing (W m^{-2})
Miller et al. (2016)	San Juan Mountains	May, 2010	Remote sensing	~37-100
Sterle et al. (2013)	eastern Sierra Nevada	Feb to May, 2009	In-situ measurements	~2.5-40
Miller et al. (2016)	San Juan Mountains	May, 2010	In-situ measurements	35-86
Dang et al. (2017)	Northern China	Jan and Feb, 2010 and 2012	In-situ measurements	7–18
	North America	Jan-Mar, 2013-2014	In-situ measurements	0.6–1.9
	The Arctic	Spring, 2005-2009	In-situ measurements	0.1–0.8
Hansen and Nazarenko (2004)	North Hemisphere		Model simulations	0.3
Qian et al. (2009)	western United States	Mar	Model simulations	~3-7
Bond et al. (2013)	Global	industrial era	Model simulations	0.13
Flanner et al. (2007)	Global	Annual 1998 (strong)	Model simulations	0.054
		Annual 2001(weak)		0.049
Qian et al. (2014)	Northeastern China	Apr	Model simulations	5-10
	North America	Apr	Model simulations	2-7

	The Arctic	Apr	Model simulations	<0.3
Zhao et al. (2014)	Northeastern China	Jan and Feb, 2010	Model simulations	10
Oaida et al. (2015)	western US	Spring, 2009-2013	Model simulations	16
Qi et al. (2017)	The Arctic	Apr, 2008	Model simulations	0.024-0.39
This study	Northeastern China	Dec-May, 2003-2018	Remote sensing	12
	NA			3.1
	Canadian Arctic			2.6
	Russian Arctic			3.3
	Greenland			1.3
	EUA			3.5